


Proteomic Analysis of the Spatio-temporal Based Molecular Kinetics of Acute Spinal Cord Injury Identifies a Time- and Segment-specific Window for Effective Tissue Repair[§]

Stephanie Devaux^{‡§§¶¶^a}, Dasa Cizkova^{§§^a}, Jusal Quanico[‡], Julien Franck[‡], Serge Nataf[¶], Laurent Pays[¶], Lena Hauberg-Lotte^{||}, Peter Maass^{||}, Jan H. Kobarg^{**}, Firas Kobeissy^{‡‡}, Céline Mériaux[‡], Maxence Wisztorski[‡], Lucia Slovinska[§], Juraj Blasko[§], Viera Cigankova^{§§}, Isabelle Fournier[‡], and  Michel Salzet^{**}

Spinal cord injury (SCI) represents a major debilitating health issue with a direct socioeconomic burden on the public and private sectors worldwide. Although several studies have been conducted to identify the molecular progression of injury sequel due from the lesion site, still the exact underlying mechanisms and pathways of injury development have not been fully elucidated. In this work, based on OMICs, 3D matrix-assisted laser desorption ionization (MALDI) imaging, cytokines arrays, confocal imaging we established for the first time that molecular and cellular processes occurring after SCI are altered between the lesion proximity, *i.e.* rostral and caudal segments nearby the lesion (R1-C1) whereas segments distant from R1-C1, *i.e.* R2-C2 and R3-C3 levels coexpressed factors implicated in neurogenesis. Delay in T regulators recruitment between R1 and C1 favor discrepancies between the two segments. This is also reinforced by presence of neurites outgrowth inhibitors in C1, absent in R1.

Moreover, the presence of immunoglobulins (IgGs) in neurons at the lesion site at 3 days, validated by mass spectrometry, may present additional factor that contributes to limited regeneration. Treatment *in vivo* with anti-CD20 one hour after SCI did not improve locomotor function and decrease IgG expression. These results open the door of a novel view of the SCI treatment by considering the C1 as the therapeutic target. *Molecular & Cellular Proteomics* 15: 10.1074/mcp.M115.057794, 2641–2670, 2016.

Spinal cord injury (SCI)¹ belongs to the serious, currently incurable disorders of the central nervous system (CNS), that are often accompanied by a permanent disability (1). Most SCI are related to traumatic spinal cord damages induced by road trauma, falls, or sport injuries (diving). Among the hallmark features of SCI is the axonal disruption in the spinal cord, which is often caused by fractured intervertebral disc or vertebrae. This primary event is followed by a progressive cascade of secondary deleterious reactions spreading to the adjacent spared tissue leading to a worsening of the neurological status (2, 3). Although axonal regeneration is initiated, it is hampered by a combination of local factors that include severe inflammation, lack of trophic support and development of an inhibitory scar-forming environment. In fact, the regenerative capacity of the central nervous system is particularly challenged in SCI as multiple cues converge to act as a chemical and physical barrier for the repair process (4, 5). It is now acknowledged that inflammation is one of the major key player that determines abortive axonal repair in SCI. Thus, although the immune response is recognized as primordial to preserve tissue homeostasis, the spatio-temporal course of inflammation in SCI is not favorable to axonal regeneration.

Acute inflammation develops hours to days following initial spinal cord trauma and is triggered by the axonal damage and

From the [‡]Univ. Lille, Inserm, U-1192 - Laboratoire Protéomique, Réponse Inflammatoire et Spectrométrie de Masse-PRISM, F-59000 Lille, France; [§]Institute of Neurobiology, Slovak Academy of Sciences, Center of Excellence for Brain Research, Soltesovej 4–6 Kosice, Slovakia; [¶]Inserm U-1060, CarMeN Laboratory, Banque de Tissus et de Cellules des Hospices Civils de Lyon, Université Lyon-1, France; ^{||}Center for industrial mathematics, University of Bremen, Bibliothekstraße 1, MZH, Room 2060, 28359 Bremen, Germany; ^{**}Steinbeis Innovation Center SCiLS Research, Fahrenheitstr. 1, 28359 Bremen, Germany; ^{‡‡}Department of Biochemistry and Molecular Genetics, Faculty of Medicine, American University of Beirut. ^{§§}Department of Anatomy, Histology and Physiology, University of Veterinary Medicine and Pharmacy in Kosice, Komenskeho 73, 041 81 Kosice, Slovakia

Received December 29, 2015, and in revised form, May 31, 2016
 Published, MCP Papers in Press, June 1, 2016, DOI 10.1074/mcp.M115.057794

Author contributions: D.C. and M.S. designed research; S.D., D.C., J.Q., J.F., S.N., L.P., L.H., P.M., J.H.K., F.K., L.S., J.B., V.C., I.F., and M.S. performed research; S.D., D.C., J.Q., J.F., S.N., L.P., L.H., P.M., J.H.K., F.K., C.M., M.W., L.S., J.B., V.C., I.F., and M.S. analyzed data; S.D. D.C. and M.S. wrote the paper; D.C., I.F., and M.S. received funding for this project.

¹ The abbreviations used are: SCI, Spinal cord injury.

neuronal cell death at the lesion site. This is followed by a cellular and molecular inflammatory cascade that initiates the activation of resident glial cells (microglia, astrocytes), infiltration of blood-borne immune cells (lymphocytes, monocytes), and a massive release of chemokines/cytokines by microglia, macrophages and neuronal cells. During the acute inflammatory response, macrophages/microglia phagocytose cell debris and also release neurotoxic factors and stimulate the formation of a glial scar that, on the long-term, prevents axonal regrowth. At this stage, a resolution of acute inflammation and a switch toward a neuroprotective cytokines/chemokines profile would favor tissue repair and limit glial scar extension. Instead, a chronic inflammatory process usually develops weeks after trauma and leads to both an aberrant tissue remodeling and a defective tissue repair. Interestingly, although there is currently no efficient therapy for SCI, one of the approved clinical treatments in the early phase of SCI is the administration of methylprednisolone treatment in order to prevent edema and to modulate inflammation (6). However, high-dose methylprednisolone is often associated with severe immunosuppression and side effects, such as pulmonary or urinary tract infections. Thus, there is an urgent need for identifying and testing novel neuro-therapeutic strategies that could prevent inflammation, limit scar extent, and stimulate tissue repair process.

In this context, a large array of molecules and therapies has been tested experimentally with the goal of targeting the healthy tissue adjacent to spinal cord lesion. Such a strategy is aimed at not only protecting this spared tissue from secondary lesion but also stimulating its regenerative potential in order to promote neuronal networks connectivity and axonal outgrowth. Among these proposed therapeutic strategies, cellular therapy belongs to the promising candidate approaches. Ideally, cell therapy strategies may allow to: (1) bridge spinal cord segments over any cavities or cysts formed at the lesion site, (2) replace lost neurons, oligodendroglia, and (3) create a favorable environment for axonal regeneration (7). Different cell therapy approaches include embryonic stem cells, induced pluripotent stem cells (iPS) and different categories of adult stem cells and progenitors such as olfactory ensheathing stem cells, neural progenitor cells (NPC) and mesenchymal stem cells (MSCs). In addition, graft of activated macrophages and transplantation of peripheral or central nervous tissue have been also proposed as an alternative to these stem cells based treatments (8). Comparative to cell therapy, other approaches including the use of exogenously-delivered neuroprotective molecules that would protect neurons from deleterious secondary processes, promote axonal growth and/or enhance nerve conduction in the preserved or regenerating axons. Different classes of molecules were shown to afford variable levels of clinical recovery in animal models of SCI. These comprise anti-inflammatory compounds such as minocycline, neurotrophic factors (BDNF, GDNF, NGF, erythropoietin) and molecules that alleviate re-

generating axons from the inhibitory effects of extracellular matrix molecules (9, 10). In particular, chondroitinase ABC eliminates chondroitin sulfate proteoglycans (CSPG) that interact with the major membranous component NG2 and inhibit the regeneration of damaged axons (11). Also, Nogo-A is one of several neurite growth inhibitory receptors expressed by axons (12). Thereby Nogo neutralizing antibodies or blockers of the post-receptors components of RhoA are used to improve long-distance axon regeneration and sprouting (13). Of note, Rho pathway is important to control the neuronal response after CNS injury and the RhoA inhibitor cethrin is actually in phase I/II a clinical trial (14). However, although numerous therapies exhibit potentials to foster neuroprotection, stimulate neurite outgrowth and reduce inflammation, the translation to clinical side is still not crowned by success. Reasons for such a failure are multiple and reside notably in our relatively poor knowledge on the spatiotemporal kinetics of secondary molecular events that characterize the post-trauma phase. This holds particularly important with regard to inflammatory mechanisms that may greatly vary depending on the time point and spinal cord segment considered. Defining a time- and segment-specific window for effective treatment is a key knowledge for an appropriate neuro-therapeutic intervention.

In this work, we present the first exhaustive spatio-temporal proteomic and biochemical analysis performed along the entire spinal cord axis in rat model of SCI. We combined this global proteomic analysis with 3D molecular mass spectrometry imaging study, time course analysis of immune cells infiltration and cytokine microarrays quantification. The whole spectrum of the data allowed us to depict a complete scheme along the spinal cord axis of the cellular and molecular sequel of events occurring through the time course of inflammatory process and abortive regeneration. We identified specific markers for each segment at different time points (3, 7, and 10 days) of the biochemical-pathophysiological processes and observed that, surprisingly, segments caudal to the lesion site host a robust inflammatory process accompanied by the local synthesis of neuroprotective and regenerative molecules. In particular, we demonstrated that the caudal segment immediately adjacent to the lesion site possesses, at least temporarily, all the intrinsic components/features that may allow axonal regeneration to occur. Such a caudal-to-rostral altered regenerative potential is likely hampered by inhibitory signals such as glycans that are abundantly detected or even secreted at the lesion site. Finally, we provided evidence that immunoglobulins (IgGs) are present at the lesion site only 3 days after injury and that *in vivo* treatment of anti-CD20 did not diminish the presence of these antibodies and did not ameliorate the BBB score of the treated animals.

EXPERIMENTAL PROCEDURES

Reagents—Dulbecco's modified Eagle's medium (DMEM) media, phosphate buffer saline (PBS), fetal calf serum (FCS) were purchased

from Invitrogen Life Technologies (Milan, Italy). Rat Cytokine Array Panel A was from R&D Systems (Minneapolis, MN). All chemicals were of the highest purity obtainable. Water, formic acid (FA), trifluoroacetic acid (TFA), acetonitrile (AcN) were purchased from Biosolve B.V. (Valkenswaard, The Netherlands). DL-dithiothreitol (DTT), Thiourea and iodoacetamide (IAA) were purchased from SIGMA (Saint-Quentin Fallavier, France). Trypsin/Lys-C Mix, Mass Spec Grade was purchased from Promega (Charbonnières, France) and Dynabeads® Protein A from Novex (Life Technologies, France). Fluorescence conjugated secondary antibodies and DAPI were purchased from MolecularProbes (Eugene, OR).

Animals—The study was performed with approval and in accordance to the guidelines of the Institutional Animal Care and Use Committee of the Slovak Academy of Sciences and with the European Communities Council Directive (2010/63/EU) regarding the use of animals in Research, Slovak Law for Animal Protection No. 377/2012 and 436/2012.

Experimental Design and Statistical Rational—For the collection of the conditioned media $n = 3$ rats control (no balloon inflation, 0 day) were sacrificed, $n = 3$ rats after 3 days SCI, $n = 3$ rats after 7 days post injury and $n = 3$ rats after 10 days post SCI. For the control group all segments are in triplicate. For the group 3 days after SCI, R3 and C3 segments include 2 replicates and $n = 3$ for the other segments. For the group 7 days after SCI R3 and C3 segments include 2 replicates and $n = 3$ for the other segments. For the group 10 days post SCI all segments are in triplicate. For the cytokines arrays experiments $n = 1$ rat were sacrificed per condition. The experiments were performed in experimental replicates. For the IgG purification $n = 3$ rats per condition (control, 3, 7, and 10 days) were sacrificed. The experiments were performed in biological replicates. For the immunohistochemistry experiments $n = 3$ rats per condition were sacrificed. The analyses were performed in biological triplicates. For MALDI imaging experiment $n = 1$ rat was sacrificed 3 days post injury. Twenty-five sections for the complete 3D MALDI imaging experiments have been performed from R1 to C1.

Statistical analysis: For the proteomic statistical analysis of conditioned media, only proteins presenting as significant by the ANOVA test were used with FDR 5%. Normalization was achieved using a Z-score with a matrix access by rows. The immunohistochemistry statistical analyses were based on one-way ANOVA followed by Tukey Kramer test, significant values were marked * $p < 0.05$, ** $p < 0.01$, *** $p < 0.001$. Quantification analyses of immunofluorescence staining for Iba1, FoxP3 and neutrophil elastase were performed on six sections from rostral and caudal/per condition ($n = 3$ each). Error bars represent the S.E. BBB score analysis was based on one-way ANOVA test. Values of $p < 0.05$ were considered statistically significant. For the cytokines array panel, the statistical analyses were performed using Student's *t* test * $p < 0.05$, ** $p < 0.01$, *** $p < 0.001$. Error bars represent the S.E.

Experimental Spinal Cord Injury Procedure—The SCI was induced using the modified balloon compression technique in adult male Wistar rats, according to our previously published study (15). Manual bladder expression, 2 times a day, was required for 3–10 days after the injury. In the control group a 2-French Fogarty catheter was inserted at the same level of spinal cord, but the balloon was not inflated and no lesion was performed.

Collection of Conditioned Media (CM) from Control and Lesioned Spinal Cord Segments—Experimental SCI rats at 3, 7, and 10 days and sham-operated-control rats were sacrificed by isoflurane anesthesia followed by decapitation. The spinal cord was pressure expressed by injecting sterile saline (10 ml) throughout the vertebrate canal, along the caudo-rostral axis. Each spinal cord was macroscopically observed to check that lesion was well centered at the Th8-Th9 level on the longitudinal axis. Entire spinal cord was divided into

transversally sectioned slides (~1.0 cm thick each) obtained from the lesion site (Th7-Th11) and from the segments rostral (C1-Th6) and caudal (Th12-L6) to the site of injury. Slides were then chopped into 0.5 cm thick sections (2 sections per segment) and deposited into a 12-well culture plate containing 1 ml DMEM without FCS. After 24 h incubation in a humidified atmosphere with 5% CO₂ at 37 °C, 1 ml of SCI-derived conditioned media CM (CM-SCI) were collected (rostral, lesion, caudal segments) and centrifuged 30 min at 15,000 rpm at 4 °C. The same procedure was performed for obtaining CM from control spinal cord tissue. Samples were stored at –80 °C. To address the degree of cell-to cell integrity and viability, additional cryostat sections were cut from incubated segments for 24 h and immersed into tissue-tek®. Afterward cryostat sections were processed to standard IHC with NeuN and GFAP antibodies. The data confirmed the cyto- architecture of neurons and glial cells (supplemental Fig. S1) and confirmed the well preserved neuro-glial integrity within cultured spinal cord segments 24 h *in vitro*. This confirms that the collected molecules are products of vital cells processes.

Conditioned Media Digestion—A volume of 150 μ l of tissue supernatants were denatured with 2 M urea in 10 mM HEPES pH 8 by ultrasonication on ice. Protein reduction is realized by incubation with 10 mM DTT for 40 min at 56 °C followed by alkylation with 55 mM IAA for 40 min in the dark. IAA was quenched with 100 mM thiourea. Protein digestion was performed with 30 μ g/ml LysC/Trypsin mix, overnight, at 37 °C. Digestion was stopped with 0.5% TFA. The solution was dried in a SpeedVac to reduce the volume. Peptides were desalted using C18 ziptips (Millipore). Elution peptides were dried in a SpeedVac and resuspended in 0.1% FA before injecting into nanoLC.

LC MS/MS Analysis of Conditioned Media—Samples were separated by online reversed-phase chromatography using a Thermo Scientific Proxeon Easy-nLC1000 system equipped with a Proxeon trap column (100 μ m ID \times 2 cm, Thermo Scientific) and a C18 packed-tip column (Acclaim PepMap, 75 μ m ID \times 15 cm, Thermo Scientific). Peptides were separated using an increasing amount of acetonitrile (5–35% over 120 min) at a flow rate of 300 nL/min. The LC eluent was electrosprayed directly from the analytical column and a voltage of 1.7 kV was applied via the liquid junction of the nanospray source. The chromatography system was coupled to a Thermo Scientific Q-exactive mass spectrometer programmed to acquire in a data-dependent mode Top 10 most intense ion method. The survey scans were done at a resolving power of 70,000 FWHM (m/z 400), in positive mode and using an AGC target of 3e6. Default charge state was set at 2, unassigned and +1 charge states were rejected and dynamic exclusion was enabled for 25 s. The scan range was set to 300–1600 m/z . For ddMS², the scan range was between 200–2000 m/z , 1 microscan was acquired at 17,500 FWHM and an isolation window of 4.0 m/z was used.

MS Data Analysis—All the MS data were processed with MaxQuant (17) (version 1.5.1.2) using the Andromeda (18) search engine. Proteins were identified by searching MS and MS/MS data against Decoy version of the complete proteome for *Rattus norvegicus* of the UniProt database (19) (Release June 2014, 33,675 entries) combined with 262 commonly detected contaminants. Trypsin specificity was used for the digestion mode with N-terminal acetylation and methionine oxidation selected as the variable. Carbamidomethylation of cysteines was set as a fixed modification, with up to two missed cleavages. For MS spectra, an initial mass accuracy of 6 ppm was selected, and the MS/MS tolerance was set to 20 ppm for HCD data. For identification, the FDR at the peptide spectrum matches (PSMs) and protein level was set to 1%. Relative, label-free quantification of proteins was performed using the MaxLFQ algorithm (20) integrated into MaxQuant with the default parameters. The data sets and the Perseus result files used for analysis were deposited at the ProteomeXchange Consor-

tium (21) (<http://proteomecentral.proteomexchange.org>) via the PRIDE partner repository (22) with the data set identifier PXD003375. Analysis of the proteins identified was performed using Perseus software (<http://www.perseus-framework.org/>) (version 1.5.0.31). The file containing the information from identification was used with hits to the reverse database, and proteins only identified with modified peptides and potential contaminants were removed. Then, the LFQ intensity was logarithmized ($\log_2[x]$). Categorical annotation of rows was used to defined different groups after grouping replicates: (1) Temps (Control, 3, 7 and 10 days), (2) Segments (R3, R2, R1, L, C1, C2, and C3). Multiple-samples tests were performed using ANOVA test with a FDR of 5% and preserving grouping in randomization. Normalization was achieved using a Z-score with a matrix access by rows.

For the statistical analysis, only proteins presenting as significant by the ANOVA test were used for statistical analysis. Hierarchical clustering depending on time or segment was first performed using the Euclidean parameter for distance calculation and average option for linkage in row and column trees using a maximum of 300 clusters. For visualization of the variation of proteins expression depending to the condition, the profile plot tool was used with a reference profile and an automatic selection of the 10 or 15 correlated profiles. To quantify fold changes of proteins across samples, we used MaxLFQ. To visualize these fold changes in the context of individual protein abundances in the proteome, we projected them onto the summed peptide intensities normalized by the number of theoretically observable peptides. Specifically, to compare relative protein abundances between and within samples, protein lengths normalized to \log_2 protein intensities (termed “iBAQ” value in MaxQuant) were added to the MaxLFQ differences. Functional annotation and characterization of identified proteins were obtained using PANTHER software (version 9.0, <http://www.pantherdb.org>) and STRING (version 9.1, <http://string-db.org>). Using the GeneMANIA Cytoscape plugin (23), 4 co-expression networks were generated from the proteomic values obtained by the analysis of control samples and caudal, rostral and lesion segments respectively. Each segment-specific coexpression network was calculated from data obtained at all-time points following SCI. Such an approach allowed then to perform a supervised clustering in order to identify functionally-relevant subnetworks that would constitute a segment-specific and time-independent molecular signature. In particular, to identify “Inflammation” subnetworks, Fibrinogen alpha (FgA) was chosen as a reference protein and, for each group of samples, networks were built that gathered the 100 proteins whose values were the most closely correlated with those of FgA. Lists of proteins and their encoding genes were then submitted to an enrichment analysis based on gene ontology (GO) annotations, using the open source tool EnrichR (24). Finally, coexpressed proteins whose encoding genes were annotated with the same GO term of interest (for instance “complement activation”), were extracted and subnetworks visualized on cytoscape. The same method was applied to identify “axon guidance” and “neuron differentiation regulation” subnetworks from the networks of proteins coexpressed with neurofilament proteins Nfl, Nfm and Nfh in each group of samples. For presentation purposes, nodes were assigned equal weights and subnetworks were slightly distorted to avoid node superimposition.

Subnetwork Enrichment Pathway Analyses and Statistical Testing—The Elsevier’s Pathway Studio version 9.0 (Ariadne Genomics/Elsevier) was used to deduce relationships among differentially expressed proteomics protein candidates using the Ariadne ResNet-database (25, 26). “Subnetwork Enrichment Analysis” (SNEA) algorithm was selected to extract statistically significant altered biological and functional pathways pertaining to each identified set of protein hits (C1, C2, C3, R1, R2, and R3 sets). SNEA utilizes Fisher’s statistical test used to determine if there are non-randomized associations

between two categorical variables organized by specific relationship. SNEA starts by creating a central “seed” from all relevant entities in the database, and retrieving associated entities based on their relationship with the “seed” (i.e. binding partners, expression targets, protein modification targets, regulation). The algorithm compares the subnetwork distribution to the background distribution using one-sided Mann-Whitney U-Test, and calculates a p value indicating the statistical significance of difference between two distributions. In our analysis, “GenBank” ID and gene symbols from each set were imported to the software to form an experimental data set. For the reconstruction of networks of pathways, biological processes and molecular function were evaluated for each single protein hit and its associated targets (networks and pathways) (27, 28). Integrated Venn diagram analysis was performed using “the InteractiVenn”; a web-based tool for the analysis of complex data sets.

Cytokines Profile of Conditioned Medium—Cytokines and chemokines expression of CM from control, 3, 7, and 10 days for the segments R1 and C1 was performed by using a Rat Cytokine Array Panel A according to the manufacturer’s instructions. Briefly, the array membranes were first incubated in the blocking buffer for 1 h. In the meantime, 200 μ l of CM were mixed with the Detection Antibody Mixture and incubated for 1 h at room temperature. Then, after removing the block buffer, the sample/antibody mixture were added to array membranes and incubated overnight at 4 °C. After incubation, the membranes were washed 3 times with the wash buffer and then incubated with the Streptavidin-HRP solution for 30 min at room temperature. The membranes were finally washed with wash buffer for 3 times and the bound antibodies were detected by chemoluminescence using the chemireagent mix. The membranes were quantified by densitometry using ImageJ software. Background staining and spot size were analyzed as recommended by the manufacturer. Normalization was done with control expression.

IgG Purification with Dynabeads Protein A—CM (150 μ l) obtained from lesion site (~1.5 mg of protein in 2 ml) after SCI3, 7 or 10 days after SCI and from the corresponding segment of control spinal cord were bound with 50 μ l of Dynabeads Protein-A 200 μ l of PBS-Tween 20 and incubated 10 min with rotation at room temperature. The beads coupled with IgGs were harvested using a magnet (1 min) and the recovered supernatant solution was removed. The remaining beads-IgG complex was washed with PBS-Tween 20. Afterward, IgGs bound to microbeads were eluted by adding 30 μ l of 0.1 M glycine (pH 3), incubated 10 min at 70 °C temperature to dissociate the beads-IgG complex and then neutralized by adding 30 μ l of 1 M Tris-HCl (pH 8.5). Afterward, a magnet was used to remove the beads from the eluate containing IgGs. The eluate was then separated on SDS-PAGE (12% polyacrylamide gel slabs) followed by silver staining to check the bands corresponding to IgGs of the Mw of 25 kDa, 50 kDa and 75 kDa. Shot-gun mass spectrometry analysis was performed to identify the band corresponding to the appropriate Mw. Silver destaining was performed using 30 mM of potassium ferricyanide and 100 mM sodium thiosulfate (1:1) 200 μ l per band for 20 min in the dark. Bands were washed 2 times for 15 min with Milli-Q water followed by an in-gel digestion as previously described (29). The samples were reconstituted with 10 μ l of 5% AcN/0.1% FA and injected on a UPLC MS instrument. Separation was performed using an EASY-nLC 1000 UPLC (Thermo Scientific) equipped with a 75 μ m \times 2 cm Acclaim PepMap 100 pre-column with nanoViper fittings and a 50 μ m ID \times 150 mm Acclaim PepMap RSLC analytical column (Thermo Scientific). The peptides were eluted using a gradient of AcN starting from 5% to 30% over 1 h at a flow rate of 300 nl/min. The Q-Exactive instrument was set to acquire top 10 MS2. The survey scans were taken at 70,000 FWHM (at m/z 400) resolving power in positive mode and using a target of 1E6 and default charge state of +2. Unassigned and +1 charge states were rejected, and dynamic

exclusion was enabled for 30 s. The scan range was set to m/z 300–1600 m/z . For the MS2, 1 microscan was obtained at 17,500 FWHM and isolation window of 3.0 m/z , using a scan range between m/z 200–2000 m/z . Tandem mass spectra were processed with Thermo Scientific Proteome Discoverer software version 1.3. Spectra were searched against UniprotKB/Swiss-Prot (version March 2014) filtered with *Rattus norvegicus* (25678 sequences) taxonomy using the SEQUEST HT algorithm (version 1.3.0.339). The search was performed choosing trypsin as the enzyme with one missed cleavage allowed. Precursor mass tolerance was 10 ppm, and fragment mass tolerance was 0.1 Da. N-terminal acetylation; and cysteine carbamidomethylation; methionine oxidation was set as variable modifications. Peptide validation was performed with the Percolator algorithm by filtering based on a q -value below 0.01, which corresponds to a false discovery rate (FDR) of 1%. The data sets used for analysis were deposited at the ProteomeXchange Consortium (21) (<http://proteomecentral.proteomexchange.org>) via the PRIDE partner repository (22) with the data set identifier PXD004247.

Tissue Processing and Immunohistochemical Analysis of Immune Cells—Rats following SCI at 3, 7 and 10 days and sham surgery were deeply anesthetized and perfused transcardially with saline followed by 4% paraformaldehyde (PFA) in 0.1 M phosphate buffer saline. Spinal cords were removed post-fixed in 4% PFA, embedded in gelatin-egg albumin protein matrix (10% ovalbumin, 0.75% gelatin and glutaraldehyde) and soaked overnight in 30% sucrose. Each spinal cord was dissected into 1 cm block (rostral and caudal segment) and 40 μ m thick longitudinal cryostat (Leica Instruments, Heidelberg, Germany) sections (sagittal plane) were cut serially and standard immunohistochemistry technique was performed. Before incubation with primary antibodies for FoxP3 and neutrophil elastase, to reduce autofluorescence background, tissue sections were incubated 15 min at room temperature in Sudan Black B and then washed in PBS. Tissue sections were incubated in the following primary antibodies: rabbit anti-Iba1, a marker for microglia/macrophages (1:800; Wako Pure Chemical Industries, Osaka, Japan), rabbit anti-FoxP3, a marker for lymphocyte T regulator (1:200; Abcam, Cambridge, UK), rabbit anti-neutrophil elastase, a marker for neutrophil (1:200; Abcam). Tissues sections were washed in PBS and then incubated in the secondary fluorescent antibody goat anti-rabbit IgG or goat anti-mouse conjugated with AlexaFluor 594, goat anti-mouse IgG or goat anti-rabbit IgG conjugated with AlexaFluor488. Omission of the primary antibody served as the negative control. For nuclear staining, we used 4–6-diaminidino-2-phenylindol (DAPI) (1:10000). Finally, sections were washed in 0.1 M PBS, mounted, and coverslipped with Vectashield mounting medium (VectorLaboratories, Inc., Burlingame, CA) and observed under a fluorescence microscope (NikonEclipseTi, Japan) and confocal laser scanning microscope (Leica TCSSP5 AOBs, Leica Microsystems, Mannheim, Germany).

Quantification analyses of immunofluorescence staining for Iba1, FoxP3 and neutrophil elastase were performed on 6 sections from rostral and caudal/per condition ($n = 3$ each). Captured fluorescence digital images at 40x magnification were analyzed by ImageJ software. Iba1 quantification was determined by randomization counting cells manually with Image J software in gray and white matters of rostral and caudal segments. FoxP3 and neutrophil elastase quantification was determined by the percentage of positive cells compared with DAPI staining by counting cell manually with image J software.

Immunohistochemical Analysis of IgG Deposition—Tissue sections of 40 μ m thickness from rostral and caudal segment adjacent to the lesion at the 3, 7 and 10 days post-injury and corresponding cuts for controls (embedded in gelatin-egg albumin protein matrix, same procedure as for IHC for immune response) were cut. One set of tissue sections were incubated with primary goat anti-rat IgG2a antibody (1:500, Bethyl Laboratories, Inc., Montgomery, TX) overnight at 4 °C.

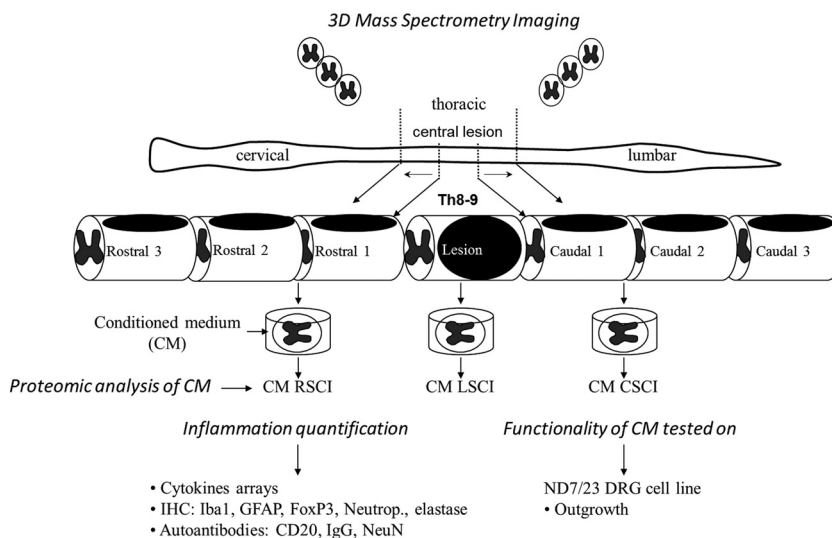
After 3 washing steps in PBS, sections were incubated with secondary fluorescent antibodies: rabbit anti-goat IgG conjugated with AlexaFluor594 or AlexaFluor 488 for one hour at room temperature. For double labeling, we have used the following primary antibodies: mouse anti-GFAP, (1/500; Upstate Biotech Millipore), rabbit anti-Iba1 (1:800), mouse anti-NeuN, marker for neurons, (1/1000; Upstate Biotech Millipore) overnight at 4 °C, followed with corresponding secondary antibodies. Another set of sections were labeled with secondary fluorescent antibody anti-rat IgG conjugated with (AlexaFluor 488), followed by incubation with primary antibodies for NeuN, GFAP and Iba1. Omission of the primary antibody served as the negative control. For nuclear staining, we used DAPI (1:10000). Finally, sections were washed with 0.1 M PBS, mounted, and coverslipped with Vectashield mounting medium and observed under a fluorescence microscope and confocal laser scanning microscope. Fluorescence or confocal images, including orthogonal views, were processed by using 0.5 μ m optical sections at 40x or 60x magnification.

Intraspinal Delivery of CD-20 Antibody—One hour after SCI, in anesthetized rats with 1.5–2% isoflurane we have microinjected intraspinally primary rabbit anti-rat CD-20 antibody (Biorbyt Ltd., Cambridge, United Kingdom), for local depletion of B- lymphocytes IgG production. Intraspinally injections of (1) saline ($n = 3$) and (2) rabbit anti-rat CD-20 antibody, 0.5 μ g/ μ l ($n = 3$) were performed using a 50- μ l Hamilton syringe (30G needle, Cole Parmer, Anjou, Quebec) connected to UltraMicroPump III with Micro4 Controller, 4-Channel (World Precision Instruments, Inc., Sarasota, FL) and stereotactic device, with a delivery rate of 0.5 μ l/min. 3 bilateral intraspinal injections of 1 μ l per injection were performed at the lesion site, whereas one injection of 1 μ l per injection was done at rostral and caudal segments. Each delivery was positioned 1 mm from the spinal cord midline and injected at a depth of 1.8–2 mm from the pial surface of the spinal cord. The distance between injections was 1 mm, avoiding vessels. Intraspinally injections were followed by procedure published in our study (16). After injecting the dose of saline or CD-20 antibody, the needle was maintained in the tissue for an additional 30 s. No antibiotic treatment was performed during animal's survival. All rats survived for 3 days.

Behavioral Testing After CD-20 Antibody Intraspinal Delivery—Animals were evaluated using Basso, Beattie, and Bresnahan (BBB) open-field test to assess motor function after SCI at day 0, 3, 7, 10, 14 and 28. Each rat was tested for 5 min by two blinded examiners. BBB test measures locomotor outcome (hind limb activity, body position, trunk stability, tail position and walking paw placement) of rats utilizing the rating scale ranges from 0 (no observable hind limbs movements) to a maximum of 21 (plantar stepping, coordination and trunk stability similar to control rats). All data are reported as mean \pm S.E. Differences in mean BBB scores between the sham-controls and SCI groups at each survival interval were assessed using one-way ANOVA.

MALDI Imaging Data Analyses—Twelve micrometer tissue sections from the R1, lesion and C1 segments were obtained using a cryostat (Leica Microsystems, Nanterre, France). These were mounted on indium tin oxide (ITO)-coated slides and placed under vacuum in a dessicator for 15 min. 2,5-dihydroxybenzoic acid was used as matrix, and was prepared at a concentration of 20 mg/ml in 70:30 methanol/0.1% TFA in H₂O. The matrix was deposited manually using a sprayer developed in-house at a flow rate of 300 μ l/h for 5 min. Lipid imaging was performed on an UltraFlex II instrument (Bruker Daltonics, Bremen, Germany) equipped with a micro-channel plate (MCP) detector. The instrument was equipped with a Smartbeam™ laser capable of operating up to 200Hz and was controlled using FlexControl 3.3 (Build 108) software (Bruker Daltonics). The data sets were recorded in positive reflector mode and 500 laser shots were accumulated for each raster point. The laser focus was set to medium, and deflection

FIG. 1. Schematic design of the experimental procedure performed in this study.



of masses was deactivated. Spectra were acquired by oversampling at a lateral resolution of $20\ \mu\text{m}$. External calibration was performed using the PepMix standard (Bruker Daltonics). Spectra were acquired between m/z 60–1000.

The 2D MALDI Imaging data of rostral (R1) caudal (C1) and lesion (L) sections after 3 days of SCI ($n = 1$) were analyzed with SCiLS Lab 2015a (30). The baseline was removed by iterative convolution and the data were normalized based on the total ion count (TIC) method (31). Subsequently, the orthogonal matching pursuit was used to detect peaks. These peaks were aligned to the mean spectrum and the data were smoothed with a strong ($\lambda = 0.5$) Chambolle filter method. Automatic spatial segmentation was performed by using the bisecting k-means algorithm (32). Colocalized m/z values with the lesion region were elucidated by using Pearson's correlation analysis. With component analysis fundamental components of given spectra and m/z images can be discovered unsupervised. Here, the principal component analysis as well as the probabilistic latent semantic analysis were used (33). The PLSA was performed with random initialization with a threshold of 29.0588, maximum interval processing mode, lower m/z range threshold mode and individual spectrum mode. The PCA was performed with no scaling, a threshold of 29.0588, maximum interval processing mode, lower m/z range threshold mode and individual spectrum mode (30).

RESULTS

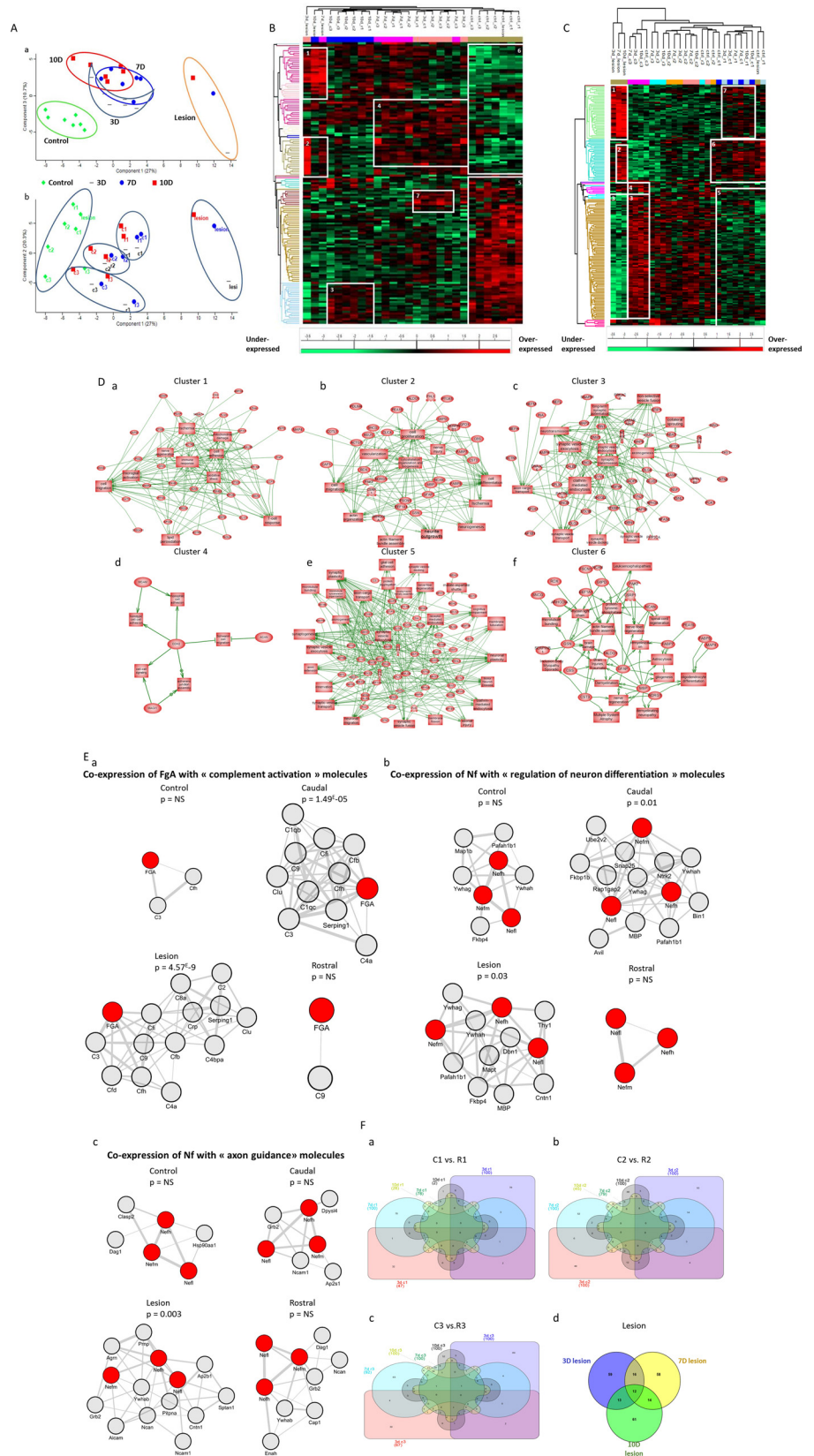
Workflow—Our main goal was to establish a fine mapping of the molecular events that occur in a time- and segment-specific manner during sub-acute SCI. We chose to focus our analysis on the identification of soluble factors that may support intra- or intersegmental communications between distinct cellular compartments. For this purpose, we performed proteomic shot-gun triplicate analyses of the conditioned medium (CM) derived from seven spinal cord segments localized at the lesion site (L) or either caudal to the lesion (C1, C2, C3) or rostral (R1, R2, R3) to the lesion. Each of these analyses were performed on spinal cord segments obtained on days 3, 7, or 10 post-SCI giving rise to a set of 80 proteomic data covering an average of 1500 proteins identified per sample with at least 2 peptides per protein recognized and percentage of false positive (FDR) $< 1\%$ (supplemental Data S1).

Proteomic data were then analyzed using complementary bioinformatics approaches that allowed unsupervised or supervised clustering of quantified proteins and the identification of differentially expressed molecules. Thus, both a comprehensive strategy without *a priori* and a focused one were applied to analyze proteomics data. In parallel, cytokine array measurements were performed and the whole of the proteomics data obtained from supernatant analyses was then correlated with immunohistological analyses and functional studies (Fig. 1).

Global Proteomic Study Along the Spinal Cord Axis at Key Time Points of SCI—Principal component analysis of conditioned media proteomics data clearly demonstrated that profiles in SCI samples can be clustered depending on the segment localization, irrespective of the time point considered. In addition, control samples harbor a molecular profile that can be sharply distinguished from any of SCI profiles, including those of segments localized at distance from the lesion site (*i.e.* the R3 and C3 profiles) (Fig. 2A). Time course analyses show that control samples, in one hand, and lesion samples, on the other hand, are clearly distant from all other samples (Fig. 2Aa upper panel). The remaining profiles display a partial overlap, indicating that time point may not be the main parameter allowing discriminating the proteomic profiles of spinal cord segments in this model. In contrast, a clear clustering of profiles was obtained when analyzing samples on the basis of their spatial localization (Fig. 2Ab lower panel). Thus, independently from the time point considered, profiles from each group of segments analyzed (*i.e.* rostral *versus* caudal *versus* lesion) displayed intragroup similarities. This finding provides evidence that in the SCI model, proteomic profiles in spinal cord segments may be discriminated on the basis of spatial localization. This result also demonstrates that with regard to the secretome, spinal cord segments tend to coevolve in function of their distance to the lesion site rather than their caudal *versus* rostral localization. Indeed, in terms of proteins

FIG. 2. Spatio-temporal organization of proteins.

A, Principal component analysis (PCA) of conditioned media shows the representation of the different samples grouping regarding (a) time after injury and (b) spatial organization of the spinal cord. One point corresponds to all proteins identified according to their label free quantification for each segments and each time point. Heat map of proteins with different secretion profiles in conditioned media from different time after SCI (3D, 7D, 10D, and control) and from different segments (R3, R2, R1, L, C1, C2, C3). **B**, Hierarchical clustering regarding time point. **C**, Hierarchical clustering regarding spatial organization. Distinct clusters are highlighted. **D**, System biology analysis for network identification in each cluster issued from heat map of proteins with different secretion profiles in conditioned media from different time after SCI (3D, 7D, 10D, and control) and from different segment (R3, R2, R1, L, C1, C2, C3) regarding the spatial organization. **E**, Analysis of coexpression networks identify in inflammation, neuro-axonal and axonal guidance in conditioned media. The 100 genes which encoded molecules were the most tightly coregulated with fibrinogen- α (FgA), neurofilament L, M and H (Nf) respectively in conditioned media control, rostral, lesion and caudal were identified and assessed for gene set enrichment. Panel **Ea** shows subnetworks of genes annotated by the GO terms “inflammation”, caudal and lesion segments have significant p value unlike control and rostral segments. Panel **Eb** presents subnetworks of genes annotated by the GO terms “neuro-axonal,” caudal and lesion have significant p value unlike control and rostral segments. Panel **Ec** shows subnetworks of genes annotated by the GO terms “axonal guidance”, only lesion has significant p value unlike caudal, lesion and rostral segments. **F**, Differential distribution of unique and common/intersected biological and functional pathways among the three spinal cord rostral and caudal regions (C1, C2, C3 versus R1, R2, and R3) factored by time of SCI (3, 7, and 10 days). Each pair of spinal cord region (C1 versus R1) was analyzed across the three time points represented utilizing a comprehensive Venn analysis representation extracted from Subnetwork Enrichment Analysis.



patterns, R3 and C3 samples cosegregated and were clearly distinguished from the R2 and C2 patterns, the R1 and C1 patterns and the lesion patterns.

Hierarchical clustering depending on the time course post-injury (Fig. 2B, Table I) or the spatial localization along the spinal cord (Fig. 2C, Table II, [supplemental Data S2](#)) were first performed using the Euclidean parameter for distance calculation and average option for linkage in row and column trees using a maximum of 300 clusters. As a criterion of significance, we applied an ANOVA significance threshold of $p < 0.05$, and heat maps were created. A total of 147 proteins for time-dependent clustering and 193 proteins for segment-dependent clustering were considered reliable based on statistical analysis. In the time-dependent clustering (Fig. 2B, Table I), two major branches of the heat map separated the 3 day lesion segment in one branch from the others in the second branch. This latter was subdivided in two sub-branches: the first one gathering all controls whatever the segments and the second one all the other ones. This branch was itself subdivided in 4 branches, *i.e.* one for the lesion segments and the three other ones regroup all segments per time. Overall, this approach allowed a total of 6 clusters to be retrieved (Fig. 2B, Table I). The proteins in each cluster were then analyzed using PANTHER software (<http://www.pantherdb.org>) to determine the biological functions based on the protein classes. Control group were found to be characterized by two different clusters, *i.e.* *cluster 5* signing an overexpression of tubulins network, enzymatic metabolism network and vesicle-trafficking network and *cluster 6* corresponding to an under-expression of heat shock proteins network, neurofilaments and filamins networks and immune response factors (Table I). Lesion segments showed proteins overexpressed involved in neurogenesis, notably adducin and plectin, and in immune response (*e.g.* galectin 1 and 3, coronin) (*cluster 1*) (Table I). *Cluster 2* corresponds to a clear increased expression of proteins involved in inflammation in the lesion segment after 3 days and a weak overexpression of these proteins at 7 days in the lesion segment as well as in other segments at 3 and 7 days (Table I). By comparison, inflammatory molecules were down-regulated in all segments at 10 days after SCI and in control samples. *Cluster 4* corresponds to an overexpression of proteins in rostral and caudal segments on day 3 and day 7 post-SCI. *Cluster 4* shows an overexpression of proteins involved in neurite outgrowth like SPARC, neurofilament, lamin and the ones involved in regeneration processes, but are underexpressed in control (*cluster 6*). Some proteins involved in these functions are found at 10 days overexpressed as CRMP-3 and transgelin 3, but these proteins are also present in control (Table I).

For the second clustering analysis taking into account the spatial distribution of proteins (Fig. 2C, Table II, [supplemental Data S2](#)), we observed again that the lesion segments were clustered apart from the other groups of samples. The second branch is subdivided in two branches, *i.e.* one separating C3

at each time point from the others which are then subdivided again in two branches, *i.e.* one regrouping R3 (3 and 7 days after SCI) and the other one including segments with 2 major groups (R1 and C1 *versus* R2 and C2). In the lesion segments, proteins overexpressed are related to the immune response (Table II). These proteins are also expressed in R1 and C1 segments at each time point after SCI and under-expressed in the other segments, showing the correlation between lesion and the rostral and caudal adjacent segments. A total of 7 clear clusters were identified. *Clusters 2* and *6* correspond to proteins overexpressed in lesion and in R1, C1, respectively, and include proteins involved in neurite outgrowth but also inhibitors of neurite outgrowth such as neurocan (Table II). These proteins are expressed in lesion after 7 and 10 days and also in segments R1 and C1 for each time point. Some proteins involved in neurite outgrowth are present in C3 segment but some are inhibitory like aggrecan protein. Proteins involved in neurogenesis and synaptogenesis are overexpressed in C3 segments, with lower expression in segments R3, R2, and C2 and under-expressed in lesion, R1 and C1 segments (*cluster 3* and *cluster 5*). However, some neurite inhibitors are also present (Table II). For a more detailed analysis, we performed a systems biology analysis for network identification in each cluster identified in the segment-dependent clustering analysis (Fig. 2D, Table II). Differential pathways were generated using the “direct interaction” algorithm to map the functional relationships linking the identified proteins in each cluster. Regarding clusters identified as overexpressed in the lesion segment, the protein network formed by *cluster 1* is implicated in immune response (*i.e.* cell migration, microglia activation and T cell response) as well as nerve regeneration whereas *cluster 2* forms a protein network involved in neurite outgrowth, nerve regeneration, cell migration and cytoskeleton remodeling (Figs. 2Da and 2Db). By contrast, *cluster 3*, which corresponds to proteins under-expressed in lesion segment, is functionally related to synaptic functions and axonogenesis and collateral sprouting (Fig. 2Dc). *Cluster 4* corresponds to proteins overexpressed in C3 segment and functionally associated with cell-adhesion N-cadherin-related functions involving notably aggrecan, and CD146 (Fig. 2Dd). *Clusters 5 and 6* are formed by overexpressed proteins in both R1 and C1 segments. *Cluster 5* is related to synaptogenesis, axon extension, and neuronal plasticity (Fig. 2De) whereas *cluster 6* is linked to demyelination, oligodendrocytes differentiation, astrogliosis, and nerve regeneration, (Fig. 2Df). Overall, these clustering analysis data confirmed that (1) the lesion site is the most divergent from the other segments in terms of nature and functions of protein networks and (2) secretome profiles of spinal cord segments tend to coevolve depending on their relative distance to the lesion site (*i.e.* R3 with C3, R2 with C2, R1 with C1).

However, besides similarities, differences could be also identified between segments located at equidistance from the

TABLE I

List of proteins identified by cluster after perseus analyses taking into account the time course

Time clustering		
Accession number	Protein name	Gene name
Cluster 1		
O08557	N(G),N(G)-dimethylarginine dimethylaminohydrolase 1	Ddah1
P02650	Apolipoprotein E	ApoE
P06761	78 kDa glucose-regulated protein	Hspa5
P08699	Galectin-3	Lgals3
P09495	Tropomyosin alpha-4 chain	Tpm4
P10960	Sulfated glycoprotein 1	Psap
P11598	Protein disulfide-isomerase A3	Pdia3
P11762	Galectin-1	Lgals1
P30427	Plectin	Plec
P31000	Vimentin	Vim
P31232	Transgelin	Tagln
G3V913	Heat shock 27kDa protein 1	Hspb1
P55051	Fatty acid-binding protein, brain	Fabp7
P85972	Vinculin	Vcl
Q5RK10	WD repeat-containing protein 1	Wdr1
Q5XF0	Transgelin-2	Tagln2
Q63610-2	Tropomyosin alpha-3 chain	Tpm3
Q6JE36	Protein NDRG1	NdrG1
Q9WV7	Protein phosphatase 1F	Ppm1f
B0K010	Protein Txndc17	Txndc17
C0JPT7	Filamin alpha	Flna
D3ZHA0	Protein FlnC	FlnC
D3ZQP6	Protein Sema7a	Sema7a
G3V852	Protein Tln1	Tln1
G3V8L3	Lamin A, isoform CRA_b	Lmna
G3V940	Coronin	Coro1b
Q5X138	Lymphocyte cytosolic protein 1	Lcp1
Cluster 2		
B0BNN3	Carbonic anhydrase 1	Ca1
P01048	T-kininogen 1	Map1
P02091	Hemoglobin subunit beta-1	Hbb
P02680-2	Fibrinogen gamma chain	Fgg
P04639	Apolipoprotein A-I	Apoa1
P06238	Alpha-2-macroglobulin	A2m
P06866	Haptoglobin	Hp
P08932	T-kininogen 2	
P14480	Fibrinogen beta chain	Fgb
P17475	Alpha-1-antiproteinase	Serpina1
P20059	Hemopexin	Hpx
Q63041	Alpha-1-macroglobulin	A1m
Q9QX79	Fetuin-B	Fetub
G3V7K3	Ceruloplasmin	Cp
M0RBF1	Complement C3	C3
O54854	Kallikrein 6, isoform CRA_a	Klk6
Q5EBC0	Inter alpha-trypsin inhibitor, heavy chain 4	Itih4
Q5M7T5	Protein Serpinc1	Serpinc1
Q62669	Protein Hbb-b1	Hbb-b1
Q68FY4	Group specific component	Gc
Q7TQ70	Ac1873	Fga
Cluster 3		
B0BNM1	NAD(P)H-hydrate epimerase	Apoa1bp
B2RYG6	Ubiquitin thioesterase OTUB1	Otub1
P05544	Serine protease inhibitor A3L	Serpina3l
P10860	Glutamate dehydrogenase 1, mitochondrial	Glud1
P11030	Acyl-CoA-binding protein	Dbi
P37805	Transgelin-3	Tagln3
P50398	Rab GDP dissociation inhibitor alpha	Gdi1
P62161	Calmodulin	Calm1
P63086	Mitogen-activated protein kinase 1	Mapk1
Q4KM74	Vesicle-trafficking protein SEC22b	Sec22b

TABLE I—continued

Time clustering		
Accession number	Protein name	Gene name
Q4KMA2	UV excision repair protein RAD23 homolog B	Rad23b
Q62952-2	Dihydropyrimidinase-related protein 3	Dpysl3
Q6AY84	Secernin-1	Scrn1
Q7TP98	Interleukin enhancer-binding factor 2	Ilf2
D4A5X8	Protein Ahcy1	Ahcy1
F1M978	Inositol monophosphatase 1	Impa1
F1M9V7	Protein Npepps	Npepps
F1MAQ5	Microtubule-associated protein	Map2
G3V8G4	Brevican, isoform CRA_a	Bcan
M0R686	Protein Irgq	Irgq
M0RE01	Uncharacterized protein	LOC100911107
Cluster 4		
B0BNN3	Carbonic anhydrase 1	Ca1
P01048	T-kininogen 1	Map1
P02091	Hemoglobin subunit beta-1	Hbb
P02680-2	Fibrinogen gamma chain	Fgg
P04639	Apolipoprotein A-I	Apoa1
P04692-5	Tropomyosin alpha-1 chain	Tpm1
P06238	Alpha-2-macroglobulin	A2m
P06866	Haptoglobin	Hp
P08592-2	Amyloid beta A4 protein	App
P08932	T-kininogen 2	
P09606	Glutamine synthetase	Glul
P11348	Dihydropteridine reductase	Qdpr
P12839	Neurofilament medium polypeptide	Nefm
P14480	Fibrinogen beta chain	Fgb
P16975	SPARC	Sparc
P17475	Alpha-1-antiproteinase	Serpina1
P19527	Neurofilament light polypeptide	Nefl
P20059	Hemopexin	Hpx
P21807	Peripherin	Prph
P34058	Heat shock protein HSP 90-beta	Hsp90ab1
P50503	Hsc70-interacting protein	St13
P62703	40S ribosomal protein S4, X isoform	Rps4x
P82995	Heat shock protein HSP 90-alpha	Hsp90aa1
Q63041	Alpha-1-macroglobulin	A1m
Q66HA8	Heat shock protein 105 kDa	Hsp1
Q9QX79	Fetuin-B	Fetub
Q9QZA2	Programmed cell death 6-interacting protein	Pdcd6ip
F1LM84	Nidogen-1	Nid1
F1LRZ7	Neurofilament heavy polypeptide	Nefh
G3V7K3	Ceruloplasmin	Cp
G3V7U4	Lamin-B1	LmnB1
Q6PDW1	40S ribosomal protein S12	Rps12
M0RBF1	Complement C3	C3
O54854	Kallikrein 6, isoform CRA_a	Klk6
Q5EBC0	Inter alpha-trypsin inhibitor, heavy chain 4	Itih4
Q5M7T5	Protein Serpinc1	Serpinc1
Q62669	Protein Hbb-b1	Hbb-b1
Q68FY4	Group specific component	Gc
Q6MGC4	H2-K region expressed gene 2, rat orthologue	Pfdn6
Q7TQ70	Ac1873	Fga
Cluster 5		
B0BNM1	NAD(P)H-hydrate epimerase	Apoa1bp
B2RYG6	Ubiquitin thioesterase OTUB1	Otub1
O08651	D-3-phosphoglycerate dehydrogenase	Phgdh

TABLE I—continued

Time clustering		
Accession number	Protein name	Gene name
O35077	Glycerol-3-phosphate dehydrogenase [NAD(+)], cytoplasmic	Gpd1
O35760	Isopentenyl-diphosphate Delta-isomerase 1	Idi1
O88350	Putative hydrolase RBBP9	Rbbp9
M0R590	Protein LOC685186	LOC685186
P04905	Glutathione S-transferase Mu 1	Gstm1
F1LND7	Farnesyl pyrophosphate synthase	Fdps
P05544	Serine protease inhibitor A3L	Serpina3l
P05708	Hexokinase-1	Hk1
P08009	Glutathione S-transferase Yb-3	Gstm3
P10860	Glutamate dehydrogenase 1, mitochondrial	Glud1
P10959	Carboxylesterase 1C	Ces1c
P11030	Acyl-CoA-binding protein	Dbi
P11980	Pyruvate kinase PKM	Pkm
P12346	Serotransferrin	Tf
P12785	Fatty acid synthase	Fasn
P13233	2',3'-cyclic-nucleotide 3'-phosphodiesterase	Cnp
P13668	Stathmin	Stmn1
G3V9G4	ATP citrate lyase, isoform CRA_b	Acly
P17425	Hydroxymethylglutaryl-CoA synthase, cytoplasmic	Hmgcs1
P24155	Thimet oligopeptidase	Thop1
P24329	Thiosulfate sulfurtransferase	Tst
P28037	Cytosolic 10-formyltetrahydrofolate dehydrogenase	Aldh1l1
P30904	Macrophage migration inhibitory factor	Mif
P32232-2	Cystathionine beta-synthase	Cbs
P37361	Metallothionein-3	Mt3
P37805	Transgelin-3	Tagln3
P50398	Rab GDP dissociation inhibitor alpha	Gdi1
P50408	V-type proton ATPase subunit F	Atp6v1f
P51635	Alcohol dehydrogenase [NAD(+)]	Akr1a1
P84079	ADP-ribosylation factor 1	Arf1
P62161	Calmodulin	Calm1
P62828	GTP-binding nuclear protein Ran	Ran
P63086	Mitogen-activated protein kinase 1	Mapk1
Q3KRE8	Tubulin beta-2B chain	Tubb2b
Q497B0	Omega-amidase NIT2	Nit2
Q4KM74	Vesicle-trafficking protein SEC22b	Sec22b
Q4KMA2	UV excision repair protein RAD23 homolog B	Rad23b
Q4V8C3-2	Echinoderm microtubule-associated protein-like 1	Eml1
Q5BJP9	Phytanoyl-CoA dioxygenase domain-containing protein 1	Phyhd1
Q5PQN7	Protein LZIC	Lzic
Q5XI22	Acetyl-CoA acetyltransferase, cytosolic	Acat2
Q62952-2	Dihydropyrimidinase-related protein 3	Dpysl3
Q66HG4	Aldose 1-epimerase	Galm
Q6AY84	Secernin-1	Scrn1
Q6AYS7	Aminoacylase-1A	Acy1a
Q6P502	T-complex protein 1 subunit gamma	Cct3
Q6P9V9	Tubulin alpha-1B chain	Tuba1b
Q7TP98	Interleukin enhancer-binding factor 2	Ilf2

TABLE I—continued

Time clustering		
Accession number	Protein name	Gene name
Q91XU1	Protein quaking	Qki
Q9JHU0	Dihydropyrimidinase-related protein 5	Dpysl5
Q9QXU9	ProSAAS	Pcsk1n
Q9Z1B2	Glutathione S-transferase Mu 5	Gstm5
B2GUZ9	Fam49b protein	Fam49b
B4F7C2	Protein Tubb4a	Tubb4a
B5DFN4	Prefoldin 5 (Predicted), isoform CRA_a	Pfdn5
D3ZFU9	Protein Mylk	Mylk
D4AD67	Protein Ktn1	Ktn1
D4A5X8	Protein Ahcy1	Ahcy1
D4ACB8	Chaperonin subunit 8 (Theta) (Predicted), isoform CRA_a	Cct8
D4AEH9	Amylo-1, 6-glucosidase, 4-alpha-glucanotransferase (Glycogen debranching enzyme, glycogen storage disease type III)	Ag1
F1LM42	Protein Ank2	Ank2
F1M978	Inositol monophosphatase 1	Impa1
F1M9V7	Protein Npepps	Npepps
F1MAQ5	Microtubule-associated protein	Map2
F7F7H4	Uncharacterized protein	Dock2
G3V721	WW domain binding protein 2, isoform CRA_b	Wbp2
G3V7C6	RCG45400	Tubb4b
G3V8G4	Brevican, isoform CRA_a	Bcan
G3V8V3	Phosphorylase	Pygm
G3V9U0	Acyl-CoA synthetase short-chain family member 2 (Predicted)	Acss2
M0R686	Protein Irgq	Irgq
M0RE01	Uncharacterized protein	LOC100911107
Q4KM55	Protein Vta1	Vta1
Q642E5	Diphosphomevalonate decarboxylase	Mvd
Cluster 6		
B0BNN3	Carbonic anhydrase 1	Ca1
O08557	N(G),N(G)-dimethylarginine dimethylaminohydrolase 1	Ddah1
P01048	T-kininogen 1	Map1
P02091	Hemoglobin subunit beta-1	Hbb
P02650	Apolipoprotein E	Apoe
P02680-2	Fibrinogen gamma chain	Fgg
P04639	Apolipoprotein A-I	Apoa1
P04692-5	Tropomyosin alpha-1 chain	Tpm1
P06238	Alpha-2-macroglobulin	A2m
P06761	78 kDa glucose-regulated protein	Hspa5
P06866	Haptoglobin	Hp
P08592-2	Amyloid beta A4 protein	App
P08699	Galectin-3	Lgals3
P08932	T-kininogen 2	
P09495	Tropomyosin alpha-4 chain	Tpm4
P09606	Glutamine synthetase	Glul
P10960	Sulfated glycoprotein 1	Psap
P11348	Dihydropteridine reductase	Qdpr
P11598	Protein disulfide-isomerase A3	Pdia3
P11762	Galectin-1	Lgals1
P12839	Neurofilament medium polypeptide	Nefm
P14480	Fibrinogen beta chain	Fgb
P16975	SPARC	Sparc
P17475	Alpha-1-antiproteinase	Serpina1
P19527	Neurofilament light polypeptide	Nefl
P20059	Hemopexin	Hpx
P21807	Peripherin	Prph

TABLE I—continued

Time clustering		
Accession number	Protein name	Gene name
P30427	Plectin	Plec
P31000	Vimentin	Vim
P31232	Transgelin	Tagln
P34058	Heat shock protein HSP 90-beta	Hsp90ab1
G3V913	Heat shock 27kDa protein 1	Hspb1
P50503	Hsc70-interacting protein	St13
P55051	Fatty acid-binding protein, brain	Fabp7
P62703	40S ribosomal protein S4, X isoform	Rps4x
P82995	Heat shock protein HSP 90-alpha	Hsp90aa1
P85972	Vinculin	Vcl
Q5RK10	WD repeat-containing protein 1	Wdr1
Q5XF0	Transgelin-2	Tagln2
Q63028	Alpha-adducin	Add1
Q63041	Alpha-1-macroglobulin	A1m
Q63610-2	Tropomyosin alpha-3 chain	Tpm3
Q66HA8	Heat shock protein 105 kDa	Hsph1
Q68FQ2	Junctional adhesion molecule C	Jam3
Q6JE36	Protein NDRG1	Ndr1
Q9QX79	Fetuin-B	Fetub
Q9QZA2	Programmed cell death 6-interacting protein	Pdcd6ip
Q9WVR7	Protein phosphatase 1F	Ppm1f
B0K010	Protein Txndc17	Txndc17
C0JPT7	Filamin alpha	Flna
D3ZHA0	Protein FlnC	FlnC
D3ZQP6	Protein Sema7a	Sema7a
F1LM84	Nidogen-1	Nid1
F1LRZ7	Neurofilament heavy polypeptide	Nefn
G3V7K3	Ceruloplasmin	Cp
G3V7U4	Lamin-B1	Lmnb1
G3V852	Protein Tln1	Tln1
G3V8L3	Lamin A, isoform CRA_b	Lmna
G3V940	Coronin	Coro1b
Q6PDW1	40S ribosomal protein S12	Rps12
M0RBF1	Complement C3	C3
O54854	Kallikrein 6, isoform CRA_a	Klk6
Q5EBC0	Inter alpha-trypsin inhibitor, heavy chain 4	Itih4
Q5M7T5	Protein Serpinc1	Serpinc1
Q5XI38	Lymphocyte cytosolic protein 1	Lcp1
Q62669	Protein Hbb-b1	Hbb-b1
Q68FY4	Group specific component	Gc
Q6MGC4	H2-K region expressed gene 2, rat orthologue	Pfdn6
Q7TQ70	Ac1873	Fga
Cluster 7		
P05708	Hexokinase-1	Hk1
P12346	Serotransferrin	Tf
P30904	Macrophage migration inhibitory factor	Mif
Q6P502	T-complex protein 1 subunit gamma	Cct3
D4ACB8	Chaperonin subunit 8 (Theta) (Predicted), isoform CRA_a	Cct8
D4AEH9	Amylo-1, 6-glucosidase, 4-alpha-glucanotransferase (Glycogen debranching enzyme, glycogen storage disease type III)	Agl
F7F7H4	Uncharacterized protein	Dock2
G3V721	WW domain binding protein 2, isoform CRA_b	Wbp2

TABLE II

List of proteins identified by cluster after perseus analyses taking into account spatial localization

Segment clustering		
Accession number	Protein name	Gene name
Cluster 1		
P02650	Apolipoprotein E	ApoE
P04041	Glutathioneperoxidase 1	Gpx1
P04642	L-lactate dehydrogenase A chain	Ldha
P04785	Protein disulfide-isomerase	P4hb
P05197	Elongation factor 2	Eef2
P07151	Beta-2-microglobulin	B2m
P08649	Complement C4	C4
P08699	Galectin-3	Lgals3
P10960	Sulfated glycoprotein 1	Psap
P22734-2	Catechol O-methyltransferase	Comt
P23928	Alpha-crystallin B chain	Cryab
Q6P6T6	Cathepsin D	Ctsd
P31232	Transgelin	Tagln
P37397	Calponin-3	Cnn3
P62963	Profilin-1	Pfn1
P85968	6-phosphogluconate dehydrogenase, decarboxylating	Pgd
P85970	Actin-related protein 2/3 complex subunit 2	Arpc2
P85973	Purine nucleoside phosphorylase	Pnp
Q3MIE4	Synaptic vesicle membrane protein VAT-1 homolog	Vat1
Q4V7C7	Actin-related protein 3	Actr3
Q510D7	Xaa-Pro dipeptidase	Pepd
Q5M7U6	Actin-related protein 2	Actr2
Q5XF0	Transgelin-2	Tagln2
Q63716	Peroxisomal protein 1	Prdx1
Q64119	Myosin light polypeptide 6	Myl6
Q68FS4-2	Cytosol aminopeptidase	Lap3
Q6AYC4	Macrophage-capping protein	Capg
Q6B345	Protein S100-A11	S100a11
Q6MG61	Chloride intracellular channel protein 1	Clic1
Q6QON1	Cytosolic non-specific dipeptidase	Cndp2
D3ZHA0	Protein FlnC	FlnC
D3ZQP6	Protein Sema7a	Sema7a
F1LP60	Moesin	Msn
F1M5X1	Protein Rrbp1	Rrbp1
F1M983	Protein Cfh	Cfh
G3V852	Protein Tln1	Tln1
G3V8V1	Granulin, isoform CRA_c	Grn
M0R4S2	Apolipoprotein D	Apod
Q5XI38	Lymphocyte cytosolic protein 1	Lcp1
Q6IN22	Cathepsin B	Ctsb
Q6P9V7	Proteasome (Prosome, macropain) activator subunit 1	Psme1
Q63798	Proteasome activator complex subunit 2	Psme2
Cluster 2		
O35077	Glycerol-3-phosphate dehydrogenase [NAD(+)], cytoplasmic	Gpd1
P02688	Myelin basic protein	Mbp
P32232-2	Cystathionine beta-synthase	Cbs
P47819	Glial fibrillary acidic protein	Gfap
P85845	Fascin	Fscn1
B0BNA5	Coactosin-like protein	Cotl1
P05370	Glucose-6-phosphate 1-dehydrogenase	G6pdx
P14841	Cystatin-C	Cst3
P47875	Cysteine and glycine-rich protein 1	Csrp1
P55051	Fatty acid-binding protein, brain	Fabp7
P55053	Fatty acid-binding protein, epidermal	Fabp5
P55067	Neurocan core protein	Ncan
P62630	Elongation factor 1-alpha 1	Eef1a1
P63259	Actin, cytoplasmic 2	Actg1
P97584	Prostaglandin reductase 1	Ptgr1
Q08163	Adenylyl cyclase-associated protein 1	Cap1
Q4G075	Leukocyte elastase inhibitor A	Serpinh1a
Q5M7W5	Microtubule-associated protein 4	Map4

TABLE II—continued

Segment clustering		
Accession number	Protein name	Gene name
Q5U318	Astrocyticphosphoprotein PEA-15	Pea15
Q5XI73	Rho GDP-dissociation inhibitor 1	Arhgdia
Q63544	Gamma-synuclein	Sncg
Q64303	Serine/threonine-protein kinase PAK 2	Pak2
Q68FP1-2	Gelsolin	Gsn
Q6JE36	Protein NDRG1	Ndr1
Q7TP52	Carboxymethylenebutenolidasehomolog	Cmb1
Q9EQS0	Transaldolase	Taldo1
Q9WUH4	Four and a half LIM domainsprotein 1	Fhl1
D4A8F2	Protein Rsu1	Rsu1
E9PT65	ProteinRdx	Rdx
G3V8C4	Chlorideintracellularchannel 4, isoformCRA_b	Clic4
M0R4H5	PDZ and LIM domainprotein 4	Pdlim4
Cluster 3		
O08838	Amphiphysin	Amph
O08839-2	Myc box-dependent-interactingprotein 1	Bin1
O35095	Neurochondrin	Ncdn
O35179	Endophilin-A1	Sh3gl2
O35264	Platelet-activating factor acetylhydrolase IB subunit beta	Pafah1b2
O35814	Stress-induced-phosphoprotein 1	Stip1
O88989	Malatedehydrogenase, cytoplasmic	Mdh1
P00507	Aspartate aminotransferase, mitochondrial	Got2
P01830	Thy-1 membrane glycoprotein	Thy1
P04636	Malatedehydrogenase, mitochondrial	Mdh2
P07323	Gamma-enolase	Eno2
P07722	Myelin-associatedglycoprotein	Mag
P09951	Synapsin-1	Syn1
P10860	Glutamate dehydrogenase 1, mitochondrial	Glud1
P11348	Dihydropteridinereductase	Qdpr
P12839	Neurofilament medium polypeptide	Nefm
F1LNY3	Neural celladhesionmolecule 1	Ncam1
P14408-2	Fumarate hydratase, mitochondrial	Fh
P16617	Phosphoglycerate kinase 1	Pgk1
P19527	Neurofilament light polypeptide	Nefl
P21575-2	Dynammin-1	Dnm1
P22062	Protein-L-isoaspartate(D-aspartate) O-methyltransferase	Pcmt1
P23565	Alpha-intermexin	Ina
P25113	Phosphoglyceratemutase 1	Pgam1
P27605	Hypoxanthine-guanine phosphoribosyltransferase	Hprt1
P31016	Disks large homolog 4	Dlg4
P39069	Adenylate kinase isoenzyme 1	Ak1
P42123	L-lactate dehydrogenase B chain	Ldhb
P47709	Rabphilin-3A	Rph3a
P47728	Calretinin	Calb2
P47860	6-phosphofructokinase type C	Pf1k
P50554	4-aminobutyrate aminotransferase, mitochondrial	Abat
P53042	Serine/threonine-protein phosphatase 5	Ppp5c
P54690	Branched-chain-amino-acidaminotransferase, cytosolic	Bcat1
P60522	Gamma-aminobutyricacidreceptor-associatedprotein-like 2	Gabarrpl2
P61265	Syntaxin-1B	Stx1b
P61765-2	Syntaxin-binding protein 1	Stxbp1
P61983	14-3-3 protein gamma	Ywhag
P62632	Elongation factor 1-alpha 2	Eef1a2
P62762	Visinin-likeprotein 1	Vsn11
P62815	V-type proton ATPase subunit B, brainisoform	Atp6v1b2
P62959	Histidine triadnucleotide-binding protein 1	Hint1
P62966	Cellular retinoicacid-binding protein 1	Crabp1
P63018	Heatshockcognate 71 kDa protein	Hspa8
P63041	Complexin-1	Cplx1
P63329-2	Serine/threonine-protein phosphatase 2B catalyticsubunit alpha isoform	Ppp3ca

TABLE II—continued

Segment clustering		
Accession number	Protein name	Gene name
P86252	Transcriptionalactivatorprotein Pur-alpha (Fragments)	Pura
Q05140-2	Clathrincoatassemblyprotein AP180	Snap91
Q07266-2	Drebrin	Dbn1
Q07310-14	Neurexin-3	Nrxn3
Q5GFD9	Protein IMPACT	Impact
Q5HZA6-2	Prolylendopeptidase-like	Prepl
Q5XIT1	Microtubule-associatedprotein RP/EB familymember 3	Mapre3
Q62717	Calcium-dependentsecretionactivator 1	Cadps
Q62813	Limbic system-associated membrane protein	Lsmp
Q62910-5	Synaptojanin-1	Synj1
Q63198	Contactin-1	Cntn1
Q63560	Microtubule-associatedprotein 6	Map6
Q63622-3	Disks large homolog 2	Dlg2
Q63754	Beta-synuclein	Sncb
Q7M767	Ubiquitin-conjugating enzyme E2 variant 2	Ube2v2
Q80WA4	RNA-binding protein Nova-1	Nova1
B2GV79	Pdxpprotein	Pdxp
Q9EPH8	Polyadenylate-binding protein 1	Pabpc1
Q9ER34	Aconitate hydratase, mitochondrial	Aco2
Q9QUL6	Vesicle-fusing ATPase	Nsf
Q9QX69	LanC-likeprotein 1	Lanc1
Q9R063-2	Peroxioredoxin-5, mitochondrial	Prdx5
G3V710	Peroxioredoxin 3	Prdx3
F1LPP3	Protein kinase C and casein kinase substrate in neuronsprotein 1	Pascin1
A1L1M0	Protein kinase, cAMP-dependent, catalytic, alpha	Prkaca
B0BN63	LOC681996 protein	Ahsa1
B0BNL2	Peptidylprolyl cis/transisomerase, NIMA-interacting 1	LOC364561
B4F772	Heatshock 70 kDa protein 4L	Hspa4l
B4F7A3	Galectin	Lgalsl
D3ZC55	Heatshock 70kDa protein 12A (Predicted), isoformCRA_a	Hspa12a
D3ZCA0	Proline synthetaseco-transcribed (Predicted)	Prosc
D3ZD09	Cytochrome c oxidasesubunit 6B1	Cox6b1
D3ZNW5	Neurofascin	Nfasc
D3ZUY8	Adaptorproteincomplex AP-2, alpha 1 subunit (Predicted)	Ap2a1
D4A0I5	DnaJ (Hsp40) homolog, subfamily C, member 6 (Predicted)	Dnajc6
D4A133	Protein Atp6v1a	Atp6v1a
D4A6C9	Protein Tom1l2	Tom1l2
D4A8U7	Dynactin 1, isoformCRA_a	Dctn1
F1LRL9	Microtubule-associatedprotein 1B	Map1b
F1LRZ7	Neurofilament heavy polypeptide	Nefh
F1MAQ5	Microtubule-associatedprotein	Map2
F7EYB9	ProteinOmg	Omg
G3V758	Contactin 2	Cntn2
G3V774	F-box onlyprotein 2	Fbxo2
G3V7L8	ATPase, H+ transporting, V1 subunit E isoform 1, isoformCRA_a	Atp6v1e1
G3V936	Citrate synthase	Cs
G3V964	Neurotrimin	Ntm
G3V9N8	AP-1 complexsubunit beta-1	Ap1b1
M0RC65	Cofilin 2, muscle (Predicted), isoformCRA_b	Cfl2
Q52KS1	6-phosphofructokinase	Pfkm
Q5BJT9	Creatine kinase, mitochondrial 1, ubiquitous	Ckmt1b
Q5PQK2	Fusion, derivedfrom t(1216) malignantliposarcoma (Human)	Fus
Q6AY48	Poly(RC) binding protein 3	Pcbp3
Q6AYU5	Poly(RC) binding protein 2	Pcbp2
Cluster 4		
P51635	Alcoholdehydrogenase [NADP(+)]	Akr1a1
Q4V898	RNA-binding motif protein, X chromosome	Rbmx

TABLE II—continued

TABLE II—continued

Segment clustering		
Accession number	Protein name	Gene name
Q9EPF2-2	Cell surface glycoprotein MUC18	Mcam
Q9QXU9	ProSAAS	Pcsk1n
G3V803	Cadherin-2	Cdh2
B2GUZ9	Fam49b protein	Fam49b
P07897	Aggrecan core protein	Acan
F1M7H7	Membrane-associated guanylate kinase, WW and PDZ domain-containing protein 1	Magi1
Cluster 5		
M0RDM4	Histone H2A	LOC680322
O08838	Amphiphysin	Amph
O08839-2	Myc box-dependent-interacting protein 1	Bin1
O35095	Neurochondrin	Ncdn
O35179	Endophilin-A1	Sh3gl2
O35264	Platelet-activating factor acetylhydrolase IB subunit beta	Pafah1b2
O35814	Stress-induced-phosphoprotein 1	Stip1
O88989	Malate dehydrogenase, cytoplasmic	Mdh1
P00507	Aspartate aminotransferase, mitochondrial	Got2
P01830	Thy-1 membrane glycoprotein	Thy1
P02680-2	Fibrinogen gamma chain	Fgg
P04636	Malate dehydrogenase, mitochondrial	Mdh2
P07323	Gamma-enolase	Eno2
P07722	Myelin-associated glycoprotein	Mag
P07897	Aggrecan core protein	Acan
P09951	Synapsin-1	Syn1
P10860	Glutamate dehydrogenase 1, mitochondrial	Glud1
P11348	Dihydropteridine reductase	Qdpr
P12839	Neurofilament medium polypeptide	Nefm
F1LNY3	Neural cell adhesion molecule 1	Ncam1
P14408-2	Fumarate hydratase, mitochondrial	Fh
P14480	Fibrinogen beta chain	Fgb
P16617	Phosphoglycerate kinase 1	Pgk1
P19527	Neurofilament light polypeptide	Nefl
P21575-2	Dynamin-1	Dnm1
P22062	Protein-L-isospartate(p-aspartate) O-methyltransferase	Pcmt1
P23565	Alpha-internexin	Ina
P25113	Phosphoglycerate mutase 1	Pgam1
P27605	Hypoxanthine-guanine phosphoribosyltransferase	Hprt1
P31016	Disks large homolog 4	Dlg4
P39069	Adenylate kinase isoenzyme 1	Ak1
P42123	L-lactate dehydrogenase B chain	Ldhb
P47709	Rabphilin-3A	Rph3a
P47728	Calretinin	Calb2
P47860	6-phosphofructokinase type C	Pfkm
P50554	4-aminobutyrate aminotransferase, mitochondrial	Abat
P51635	Alcohol dehydrogenase [NADP(+)]	Akr1a1
P53042	Serine/threonine-protein phosphatase 5	Ppp5c
P54690	Branched-chain-amino-acid aminotransferase, cytosolic	Bcat1
P60522	Gamma-aminobutyrate receptor-associated protein-like 2	Gabarapl2
P61265	Syntaxin-1B	Stx1b
P61765-2	Syntaxin-binding protein 1	Stxbp1
P61983	14-3-3 protein gamma	Ywhag
P62632	Elongation factor 1-alpha 2	Eef1a2
P62762	Visinin-like protein 1	Vsnl1
P62815	V-type proton ATPase subunit B, brain isoform	Atp6v1b2
P62959	Histidine triad nucleotide-binding protein 1	Hint1
P62966	Cellular retinoic acid-binding protein 1	Crabp1
P63018	Heat shock cognate 71 kDa protein	Hspa8
P63041	Complexin-1	Cplx1
P63329-2	Serine/threonine-protein phosphatase 2B catalytic subunit alpha isoform	Ppp3ca
P86252	Transcriptional activator protein Pur-alpha (Fragments)	Pura

Segment clustering		
Accession number	Protein name	Gene name
Q05140-2	Clathrin coat assembly protein AP180	Snap91
Q07266-2	Drebrin	Dbrn1
Q07310-14	Neurexin-3	Nrxn3
F1M7H7	Membrane-associated guanylate kinase, WW and PDZ domain-containing protein 1	Magi1
Q4V898	RNA-binding motif protein, X chromosome	Rbmx
Q5GFD9	Protein IMPACT	Impact
Q5HZA6-2	Prolyl endopeptidase-like	Prepl
Q5XIT1	Microtubule-associated protein RP/EB family member 3	Mapre3
Q62717	Calcium-dependent secretion activator 1	Cadps
Q62813	Limbic system-associated membrane protein	Lsmp
Q62910-5	Synaptotagmin-1	Synj1
Q63198	Contactin-1	Cntn1
Q63560	Microtubule-associated protein 6	Map6
Q63622-3	Disks large homolog 2	Dlg2
Q63754	Beta-synuclein	Sncb
Q6PCT3	Tumor protein D54	Tpd52l2
Q7M767	Ubiquitin-conjugating enzyme E2 variant 2	Ube2v2
Q80WA4	RNA-binding protein Nova-1	Nova1
B2GV79	Pdxp protein	Pdxp
Q9EPF2-2	Cell surface glycoprotein MUC18	Mcam
Q9EPH8	Polyadenylate-binding protein 1	Pabpc1
Q9ER34	Aconitate hydratase, mitochondrial	Aco2
Q9QUL6	Vesicle-fusing ATPase	Nsf
Q9QX69	LanC-like protein 1	Lanc1
Q9QXU9	ProSAAS	Pcsk1n
Q9R063-2	Peroxisome oxidin-5, mitochondrial	Prdx5
G3V710	Peroxisome oxidin 3	Prdx3
F1LPP3	Protein kinase C and casein kinase substrate in neurons protein 1	Pacsin1
G3V803	Cadherin-2	Cdh2
A1L1M0	Protein kinase, cAMP-dependent, catalytic, alpha	Prkaca
B0BN63	LOC681996 protein	Ahsa1
B0BNL2	Peptidylprolyl cis/trans isomerase, NIMA-interacting 1	LOC364561
B2GUZ9	Fam49b protein	Fam49b
B4F772	Heat shock 70 kDa protein 4L	Hspa4l
B4F7A3	Galectin	Lgalsl
D3ZC55	Heat shock 70 kDa protein 12A (Predicted), isoform CRA_a	Hspa12a
D3ZCA0	Proline synthetase co-transcribed (Predicted)	Prosc
D3ZD09	Cytochrome c oxidase subunit 6B1	Cox6b1
D3ZFG5	Protein Pmp2	Pmp2
G3V9C7	Histone H2B	Hist1h2bk
D3ZNW5	Neurofascin	Nfasc
D3ZUY8	Adaptor protein complex AP-2, alpha 1 subunit (Predicted)	Ap2a1
D4A0I5	DnaJ (Hsp40) homolog, subfamily C, member 6 (Predicted)	Dnajc6
D4A133	Protein Atp6v1a	Atp6v1a
D4A6C9	Protein Tom1l2	Tom1l2
D4A8U7	Dynactin 1, isoform CRA_a	Dctn1
F1LRL9	Microtubule-associated protein 1B	Map1b
F1LRZ7	Neurofilament heavy polypeptide	Nefh
F1MAQ5	Microtubule-associated protein	Map2
F7EYB9	Protein Omg	Omg
G3V6P7	Myosin, heavy polypeptide 9, non-muscle	LOC100911597
G3V758	Contactin 2	Cntn2
G3V774	F-box only protein 2	Fbxo2
G3V7L8	ATPase, H+ transporting, V1 subunit E isoform 1, isoform CRA_a	Atp6v1e1
G3V936	Citrate synthase	Cs
G3V964	Neurotrimin	Ntm
G3V9N8	AP-1 complex subunit beta-1	Ap1b1
M0RC65	Cofilin 2, muscle (Predicted), isoform CRA_b	Cfl2
Q52KS1	6-phosphofructokinase	Pfkm
Q5BJT9	Creatine kinase, mitochondrial 1, ubiquitous	Ckmt1b

TABLE II—continued

Segment clustering		
Accession number	Protein name	Gene name
Q5PQK2	Fusion, derived from t(1216) malignant liposarcoma (Human)	Fus
Q6AY48	Poly(RC) binding protein 3	Pcbp3
Q6AYU5	Poly(RC) binding protein 2	Pcbp2
Q7TQ70	Ac1873	Fga
Cluster 6		
B0BNA5	Coactosin-like protein	Cotl1
O35077	Glycerol-3-phosphate dehydrogenase [NAD(+)], cytoplasmic	Gpd1
P02688	Myelin basic protein	Mbp
P05370	Glucose-6-phosphate 1-dehydrogenase	G6pdx
P14841	Cystatin-C	Cst3
P32232-2	Cystathionine beta-synthase	Cbs
P47819	Glial fibrillary acidic protein	Gfap
P47875	Cysteine and glycine-rich protein 1	Csrp1
P55051	Fatty acid-binding protein, brain	Fabp7
P55053	Fatty acid-binding protein, epidermal	Fabp5
P55067	Neurocan core protein	Ncan
P62630	Elongation factor 1-alpha 1	Eef1a1
P63259	Actin, cytoplasmic 2	Actg1
P85845	Fascin	Fscn1
P97584	Prostaglandin reductase 1	Ptgr1
Q08163	Adenylyl cyclase-associated protein 1	Cap1
Q4G075	Leukocyte elastase inhibitor A	Serp1b1a
Q5M7W5	Microtubule-associated protein 4	Map4
Q5U318	Astrocytic phosphoprotein PEA-15	Pea15
Q5X173	Rho GDP-dissociation inhibitor 1	Arhgdia
Q63544	Gamma-synuclein	Snca
Q64303	Serine/threonine-protein kinase PAK 2	Pak2
Q68FP1-2	Gelsolin	Gsn
Q6JE36	Protein NDRG1	Ndr1
Q7TP52	Carboxymethylenebutanolidase homolog	Cmb1
D4ABI6	Protein RGD1561252	RGD1561252
Q920J4	Thioredoxin-like protein 1	Txn1l
Q9EQS0	Transaldolase	Taldo1
Q9WUH4	Four and a half LIM domain protein 1	Fhl1
B0BMX3	Protein S100a16	S100a16
D4A8F2	Protein Rsu1	Rsu1
E9PT65	Protein Rdx	Rdx
G3V8C4	Chloride intracellular channel 4, isoform CRA_b	Clic4
M0R4H5	PDZ and LIM domain protein 4	Pdlim4

lesion site. This held of particular interest when comparing R1 versus C1 segments. Indeed, as compared with the R1 profile, the C1 profile was characterized by the overexpression of inflammation markers such as fibrinogen alpha, proteins involved in demyelination and molecules either favoring axonal regeneration or inhibiting neurite outgrowth. Searching for functionally-grouped networks overrepresented in the proteins obtained from segments C3, C2, to C1, from control to 3 days, 7 days and 10 days after SCI, using ClueGO, identified leading terms mostly related to axon regeneration, synaptogenesis, extracellular matrix organization, processes in time course (Fig. 3), and thus established neuron outgrowth and regeneration processes occurring after lesion in time course. These data confirm that a neurogenesis process occurs from caudal 3 to caudal 1 after SCI in time course.

To complement these unsupervised bioinformatics analyses, we then proceeded to supervised coexpression analyses in order to confirm the unique functional profile of the caudal segments. Data obtained from our time course experiments

were classified in four groups (i.e. control, lesion, rostral and caudal) from which coexpression interactions were identified. Starting from these coexpression networks, a supervised clustering was then performed using the pro-inflammatory factor Fibrinogen alpha (FgA) as a reference molecule. Results showed that, in the lesion and caudal segments only, FgA coexpression networks were significantly enriched in molecules annotated with “complement activation” gene ontology term (Fig. 2Ea). When performing a similar supervised clustering using now the axonal Neurofilament (Nf) molecules Nfl, Nfm, and Nfh, we also found in the lesion and caudal segments only, a significant enrichment in molecules involved in the “regulation of neuron differentiation” function (Fig. 2Eb). However, a significant enrichment in molecules involved in the “axon guidance” function was observed in the lesion segments with the exception of all other segments (Fig. 2Ec). These data confirm that, although similarities can be demonstrated between segments centered by the lesion site, the caudal segments express an unexpected pro-inflammatory profile and pro-regenerative profile.

We then sought to identify specific molecules and pathways that would provide a segment and time-specific proteomic signature of SCI. To achieve this goal, we analyzed the differential distribution of unique versus common/intersected biological and functional pathways among the three spinal cord rostral and caudal regions (C1, C2, C3 versus R1, R2, R3) factored by time points post-SCI (3, 7, and 10 days). Each pair of spinal cord segments (C1 versus R1, C2 versus R2, C3 versus R3) was analyzed across the three time points and a comprehensive Venn analysis diagram extracted from Subnetwork Enrichment Analysis (SEA) was generated. From the C1 versus R1 comparisons, unique statistically significant segment- and time-specific pathways were identified that included 32 pathways for C1 on day 3, 78 pathways for R1 on day 3, 53 pathways for C1 on day 7, 78 pathways for R1 on day 7, 14 pathways for R1 on day 10 and a single pathway for C1 on day 10 (Fig. 2Fa); see supplemental Data S3 for the identity of each of the unique pathways. In Fig. 2Fb, C2 versus R2 differential pathways were analyzed across the three time points (3, 7 and 10 days). Unique statistical significant pathways were identified including 48 pathways (3days, C2), 55 pathways (3days, R2), 48 pathways (7days, C2), 52 pathways (7days, R2), 66 pathways (10 days, C2) and 36 pathways (10 days, R2); see supplemental Data S4 for the identity of each of the unique pathways. In Fig. 2Fc, C3 versus R3 differential pathways were analyzed across the three time points (3, 7 and 10 days). Unique statistical significant pathways were identified including 30 pathways (3days, C3), 69 pathways (3days, R3), 58 pathways (7days, C3); 63 pathways (7days, R3), 52 pathways (10 days, C3) and 63 pathways (10 days, R3); refer to supplemental Data S5 for the identity of each of the unique pathways. In Fig. 2Fd, Lesion-specific unique and common/intersected biological and functional pathways are analyzed across the three time points. 59, 58 and 61 unique pathways

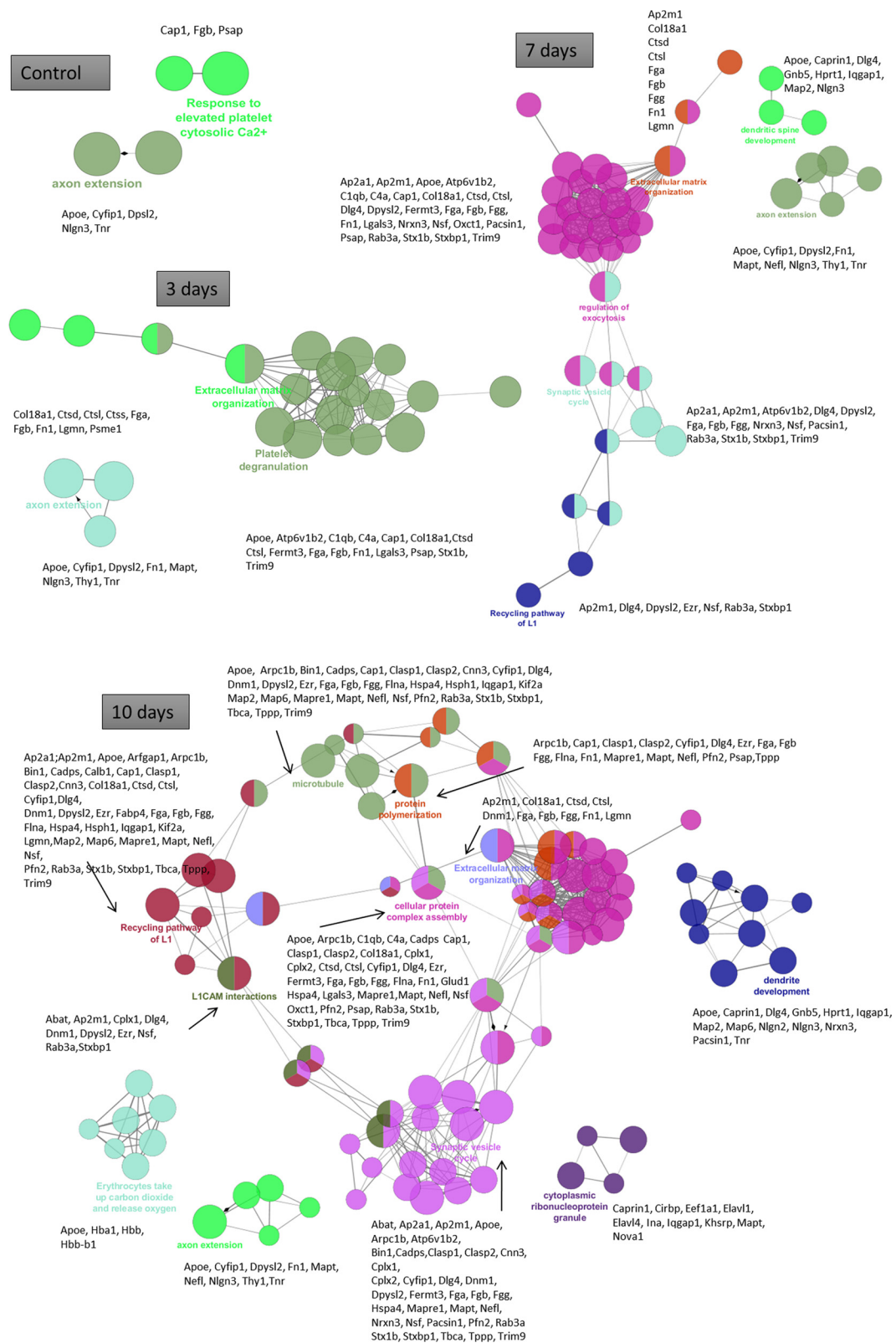


FIG. 3. ClueGo terms involved in proteins overexpressed in C3 compared with C2 and C1.

TABLE III
Specific protein per segments in time course

Segments	Protein ID	Protein Name	Identified per Time	
Lesion	G3V7H3	Cfd	3d/7d	
	P16391	RT1	3d/7d	
	P18331	Inhba	3d/10d	
	Q5FVH2	Pld3	3d/7d	
	Q62632	Fstl1	3d/10d	
	Q6P7C7	Gpnmb	3d/10d	
	B2GVB9	Fermt3	7d/10d	
	B4F7E8	Fam129b	7d/10d	
	E9PSY8	Eps15	7d/10d	
	G3V8L1	Pycard	7d/10d	
	G3V8Q0	Rgs10	7d/10d	
	P97608	Oplah	7d/10d	
	Q5BJY6	Amdhd2	7d/10d	
	Q641X3	Hexa	7d/10d	
	Q66H59	Npl	7d/10d	
	Q66HG3	Cndp1	7d/10d	
	Q6AYF2	Lmcd1	7d/10d	
	Q8K3F3	Ppp1r14b	7d/10d	
	Rostral 1	P30348	Cxcl2	3d/10d
		Q63507	Rpl14	3d/7d
Caudal 1	F1LNE5	Memo1	3d/10d	
	R9PY05	Nfasc	3d/7d	
Rostral 2	Q5U1Z2	Trappc3	7d/10d	
	G3V8D6	Trim3	3d/7d	
Caudal 2	P62836	Rap1a	3d/7d	
	Q68A21	Purb	3d/10d	
	F1LN98	Ewsr1	3d/10d	
	P0DJJ3	Sgip1	3d/7d	
	Q5X181	Fxr1	3d/7d	
Rostral 3	G3V928	Lrp1	ctrl/3d	
	D4ACV3	Hist2h2ac	3d/7d	
	F1LMU0	Myh4	3d/7d	
Caudal 3	B2GV38	Ubl4a	7d/10d	
	P45479	Ppt1	7d/10d	
	P63045	Vamp2	3d/10d	
	Q1M168	Atcay	3d/10d	
	F1LSU5	Defa10	3d/10d	
	Q920J3	Coro6	3d/10d	
	O88902	Ptpn23	3d/7d	
	D3ZH36	LOC100910536	3d/7d	

were identified corresponding to the 3 days, 7 days and 10 days' time points respectively (supplemental Data S6). Moreover, taken into account both the spatial regionalization along the spinal cord and the time course after SCI, we established that R1 versus C1 harbored no common pathways whereas R2 versus C2 shared neurites outgrowth, cell proliferation, cell differentiation, cell death and cytoskeleton organization pathways. In R3 versus C3 analyses, common pathways included cell proliferation and endocytosis pathways were found (supplemental Data S7–S9). In the same way, when taking into account the time course, 40 specific proteins unique of each segment could be retrieved, i.e. 18 specific proteins in lesion segment, 2 in R1, 2 in C1, 3 in R2, 5 in C2, 2 in R3 and 8 in C3 (Table III). Interestingly, the chemokine Cxcl2 was identified as

specific to R1, whereas in C1, Neurofascin and mediator of cell motility-1 (MEMO1). MEMO1 is implicated in a MEMO1-RhoA-DIAPH1 signaling pathway that plays an important role in ErbB2-dependent (34). Neurofascin is related to L1 family immunoglobulin cell adhesion molecule with multiple IgCAM and fibronectin domains. Neurofascin is implicated in neurite outgrowth, neurite fasciculation and organization of the axon initial segment. Importantly, Neurofascin is also targeted by autoantibodies in patients with multiple sclerosis (MS) and its altered expression has been proposed as a contributing factor to axonal pathology in MS (35). Finally, 18 lesion-specific proteins were detected among which: the follistatin-like 1 (Fstl1), a molecule that modulates the action of several growth factors on cell proliferation and differentiation and Niban-like protein 1 (Fam129b), an inhibitor of apoptosis.

Thus, these global proteomic analyses clearly demonstrate that lesion site and the proximal segments (R1 and C1) are different from the distal areas. These results are corroborated by MALDI mass spectrometry imaging (MALDI-MSI) analysis performed on R1, C1, and lesion tissues sections (Fig. 4). In fact, molecular 2D-maps based on metabolites and lipids will allow seeing the molecular regionalization in regards to physiological processes. The molecular imaging studies after SCI (3 days) show a complete disruption of gray matter-specific lipid signals along the lesion site (Fig. 4A). Spatial segmentation of MALDI-MSI data, dividing the spinal cord sections into anatomical regions allowed discriminating between different regions in an unsupervised method. The cluster analyses of rostral, lesion and caudal sections after 3 days of SCI confirm a disrupted structure of lipid distribution along the lesion site whereas the segmentation of rostral and caudal sections is consistently aligned with the spinal cord anatomy (Fig. 4B). The gray matter is shown in red and the white matter in green (Fig. 4B). *m/z* values exclusively localized with the lesion region were automatically elucidated and in Fig. 4C, 18 *m/z* images are shown. With component analysis fundamental components of the spectra and *m/z* images within the SCI MALDI-MSI data set can be discovered unsupervised. By that, the data are decomposed into a pre-specified small number of score images showing the main spatial features and a small set of component spectra showing the main spectral features. Furthermore a Receiver Operating Characteristic (ROC) analysis was performed for detecting *m/z*-values which allow a discrimination of different regions (C1 and R1); see Table IV for discriminating *m/z* values and Fig. 4Cb for a visualization of the spatial distribution of selected *m/z* values. In Fig. 4D, the results of the component analyses for the probabilistic latent semantic analysis (Figs. 4Da and 4Db) with random initialization and for principal component analysis (Fig. 4Dc) with five components are indicated. For verification of the findings obtained above, a second set of MALDI-MSI data was obtained for 24 slices of the caudal region. A 3D-visualization of selected *m/z* values, which were chosen according to the values stated in Table IV, confirms the sig-

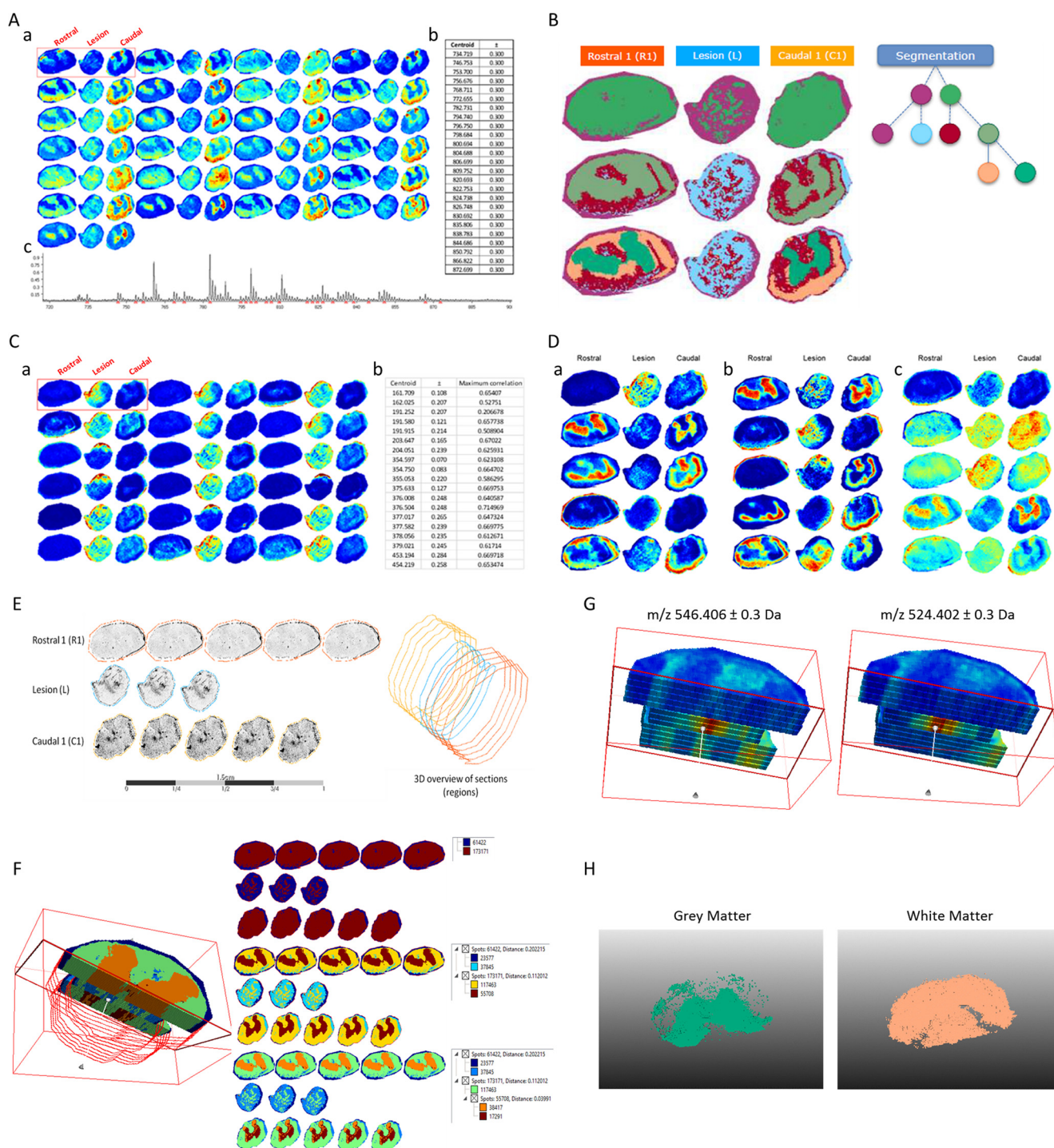


FIG. 4. A, Comparison of signals across different spinal cord segments. (a) 25 m/z image sets (left rostral, middle lesion, right caudal) are shown with ± 0.3 Da and edge-preserving image denoising as well as automatic hot spot removal. (b) The respective m/z values are indicated in the table. (c) The localization of the respective peaks is shown in the mean spectrum below. **B, Hierarchical clustering:** regions which are conjectured to be gray respectively white matter tissue is clearly structured in rostral and caudal regions, no structure visible in lesion region. **C, (a)** Colocalized m/z image sets (left rostral, middle lesion, right caudal) and (b) respective m/z values in the lesion region with the respective Pearson's correlation values. **D, Component analyses** for the probabilistic latent semantic analysis (a and b) with random initialization and principal component analysis (c) with five components. **E, 3D projection** of lipid expression across the length of spinal cord. Initial 3D alignment to follow lipid spatial distribution with imaging. **F, Cluster analyses** (segmentation) for two, four and five clusters with the respective amount of spots per cluster and the distance values to reconstruct spinal cord. **G, 3D projection** of specific signals m/z 524.402 and 546.406 detected at the lesion site. **H, 3D map** at the level of the gray and white matters of the caudal 1 segment based on 24 consecutive sections.

TABLE IV
Discriminating *m/z*-values for lesion vs. rostral/ caudal region obtained by ROC

Centroid	±	Maximum AUC	<i>m/z</i> at maximum
86.005	0.245	0.744975	86.237
86.377	0.127	0.761224	86.263
86.686	0.182	0.674034	86.517
104.076	0.277	0.734237	104.328
104.630	0.277	0.727656	104.353
169.759	0.188	0.397301	169.921
170.055	0.108	0.458626	170.150
170.271	0.108	0.759526	170.278
170.456	0.076	0.691658	170.379
170.720	0.188	0.557438	170.532
174.917	0.258	0.394923	175.163
175.398	0.223	0.739125	175.392
175.885	0.264	0.251686	176.130
184.068	0.300	0.750433	184.322
191.828	0.300	0.239038	192.108
192.352	0.163	0.737723	192.261
192.678	0.163	0.186462	192.821
213.801	0.264	0.299782	214.066
214.244	0.178	0.749835	214.244
214.636	0.214	0.50978	214.422
221.982	0.277	0.721014	222.259
222.536	0.277	0.743943	222.310
240.018	0.300	0.622719	240.298
240.629	0.300	0.755234	240.400
782.731	0.300	0.643802	782.756
783.698	0.300	0.64038	783.748
798.684	0.300	0.61345	798.735
799.702	0.300	0.616393	799.727

nificance of these molecular weights (Fig. 4E). Clustering has been performed through R1, C1, and lesion segments (Fig. 4F) and established that lesion is highly impacted compared with R1. Specific *m/z* at respectively 546.406 and 524.402 which have been retrieved at the lesion site but not in R1 and C1 segments confirm our hypothesis (Fig. 4G). In the same way, clustering analyses also allow to state that C1 is divergent from R1 (Fig. 4G). 3D map performed at the C1 segment from 24 sections showed that gray matter is more impacted compared with the white matter (Fig. 4H) and expressed specific lipids as the ones fully characterized by lipidomic in C1 and in lesion (Table V). In fact, comparison between the lesion and C1 in lipid composition showed difference in the level of expression between the two segments. These 2D- and 3D-molecular maps reinforce the proteomic analyses and point out that C1 is divergent from R1 in term of the molecular contents at different time points.

Time Course Analysis of Inflammatory and modify to regenerative Markers Along the Spinal Cord Axis—To complement the results obtained from our pan-proteomic approaches, we further focused our attention on immune and neurites outgrowth or axon guidance factors along the spinal cord in time course (Table VI). We established that, compared with control samples, immune-related proteins comprising galectins 1 and

3 (Lgals1 and 3), coronin 1b (Coro1b), macrophage migration inhibitory factor (MIF), granulin (Grn), lymphocyte cytosolic protein (Lcp1), complement system components (C3 and B2m) and cathepsins (Ctsb and Cttd), are overexpressed in the lesion site 3 days after SCI, show further increased levels at 7 days and remain at high levels at 10 days. In contrast, the inflammation peak was observed at 3 days in R1 segments and at 7 days in C1 segments. For axon guidance and neuroprojection represented by microtubule-associated protein Tau (Mapt), Pak proteins (Pak 1 and 2), Ras-related C3 botulinum toxin substrate 1 (Rac1), neural cell adhesion molecule 1 (Ncam1), stathmins (Stmn 1 and 2), semaphorin 7a (Sema7a), dectin 1 (Dctn1), neurofilament light polypeptide (Nefl), profiling 1 (Pfn1), neurofascin (Nfasc), neurotrimin (Ntm), the level of these proteins was low at 3 days, increased at 7 days and stayed stable at 10 days in the lesion segment. At 3 days, the level is the highest in C2 and C3 segments compared with C1 and R1 segments. At 7 days, it increased in C1 to C3 segments. At 10 days, it decreased in lesion, C1 and C2 segments, stayed high in C3 and increased in R1 to R3 segments. For motoneurons degeneration represented by the super dismutase 1 (Sod1), the vesicle-associated membrane protein b (Vapb), dynactin-1 (Dctn1), the highest level is in C1 to C3 segments at 7 days and in R1 to R3 segments at 10 days. For neurites inhibition, *i.e.* RhoA, neurocan (Ncan), amphiphysin (Amph), the overexpression occurs in C1 segment in time course with a peak reaching at 7 days.

In order to extend such proteomic quantitative label free results, cytokines arrays (Figs. 5A–5B) and functional assays (Figs. 5C–5E) that compared the secretome of R1 *versus* C1 segments were performed. Cytokines arrays confirmed the time-dependent and localization-dependent synthesis of chemokines and cytokines in R1 and C1 segments. Compared with control, in R1 segment, CXCL1, CXCL3, CXCL5, CCL20, TIMP-1, and IL6 are overexpressed 3 days after SCI whereas CCL3 and CTNF decrease (Fig. 5A). At 7 days after SCI, some cytokines remain high (*i.e.* CXCL1, CXCL3, and TIMP1), increase (*i.e.* CXCL2, CXCL5, CXCL7, CCL3) or remain constant (*i.e.* IL6 and CCL20) (Fig. 5A). At 10 days, CXCL1, CXCL3, CXCL2, CXCL5, and TIMP 1 fall dramatically, IL6 and CCL20 disappear and CTNF and CXCL7 continue to increase (Fig. 5A). In C1, the evolution is different (Fig. 5B). At 3 days after SCI, level of CXCL3 and TIMP-1 increase but not as registered in R1, the level of CXCL7 and CXCL5 decrease, whereas IL6 and CCL20 are not detected (Fig. 5B). After 7 days, the cytokines pattern changed with an increase of CXCL1, CXCL2, CXCL3, CXCL5, and CXCL7 levels and reapparition of IL6 together with CCL20. 10 days after SCI, CXCL1, CXCL3, CXCL5, TIMP 1 are even higher than in R1 segment and IL6 is always present in C1 but not in R1 segment. Taken together, these data showed that the cytokines pattern change in time course between R1 and C1. Specific chemokines (CXCL1, CXCL2, CXCL3, CXCL5, CXCL7, CCL3,

TABLE V
Retention time, m/z, and identification of lipids expressed in C1 or lesion segment after lipidomics analyses

Retention time (minutes) / m/z	Compound IDs	Max Fold Change	Highest Mean	Lowest Mean
46.34 / 715.4726	LMGP10010664 LMGP10010796 LMGP10010304 LMGP10010502	11	C1	lesion
52.03 / 876.6130	LMGP01030014	10	lesion	C1
44.95 / 814.5609	LMGP01012192 LMGP01011838 LMGP02010668 LMGP02010880 LMGP01011560 LMGP02010610 LMGP01011620 LMGP02011076 LMGP02010851 LMGP01011399 LMGP01011530 LMGP01010690 LMGP02010581 LMGP02010806 LMGP02010502 LMGP01012127	8	lesion	C1
48.37 / 848.5810	LMGP02030092 LMGP01030015	6	lesion	C1

CCL20, IL6) that are secreted by macrophages or epithelial cells after injury have the ability to attract neutrophils and lymphocytes, activate inflammation and stimulate extracellular matrix synthesis and tissue remodeling. This actually substantiates the hypothesis that the types of immune cells that are attracted along the spinal cord upon injury insult are quite different between rostral and caudal segments in time course, *i.e.* cells start to migrate toward R1 and then C1 segment as shown the proteomic data (Table VI). It has also to be noticed that IL6 and CCL20 are expressed firstly in R1 at 3 days after SCI and secondly appeared in C1 at 7 days. Moreover, CCL20 is also known to attract T regulator lymphocytes through CCR6 binding (36). In that context, it is necessary to correlate the cytokines expression with cellular presence in time course and along the spinal cord.

Fluorescent immunohistochemistry and cell quantification were then performed in order to compare, in C1 *versus* R1, the post-SCI time course of microglial cells, neutrophils and FoxP3 positive T regulator lymphocytes (Tregs) infiltrations (Figs. 6 and 7). Quantification of microglia revealed that the highest density of Iba-1-positive cells could be observed in gray matter areas of caudal regions, at 3 days and 7 days post-SCI (Fig. 6C). No differences are observed between the R1 and C1 segments at 10 days (Fig. 6C). As compared with control samples, Iba-1-positive microglia, in all SCI samples harbor a rounded morphology indicative of an activation state (Fig. 6). Differences between the R1 and C1 segments, with regard to microglial cells density, reach significant levels only in gray matter areas, at 3 and 7 days post-SCI (Fig. 6B–6E). Irrespective of the segment considered, the density of micro-

TABLE V—continued

Retention time (minutes) / m/z	Compound IDs	Max Fold Change	Highest Mean	Lowest Mean
44.35 / 365.3419	LMFA11000455	3	lesion	C1
40.78 / 865.5024	LMGP04010977	3	lesion	C1
	LMGP04010838			
	LMGP04010619			
51.07 / 838.5602	LMGP03010798	3	C1	lesion
	LMGP03010883			
	LMGP03010539			
54.78 / 880.6450	LMGP01090058	3	lesion	C1
	LMGP01030073			
44.35 / 838.5599	LMGP02011114	3	lesion	C1
	LMGP02010652			
	LMGP02011111			
	LMGP02010950			
	LMGP02010589			
	LMGP02010816			
40.54 / 715.5678	LMGL03012630	3	C1	lesion
40.54 / 743.5984	LMGL03012634	3	C1	lesion
45.35 / 826.5611	LMGP02010949	3	lesion	C1
	LMGP02011110			
	LMGP02010785			
	LMGP02010560			
50.09 / 850.5967	LMGP01090049	3	lesion	C1
	LMGP01090048			

glial cells decreases at 7 days but still remains above the basal microglial density observed in control samples (Fig. 6C). Results from cytokine/chemokine arrays urged us to perform a similar immunohistochemical analysis for neutrophils and Tregs. Similar study was performed for neutrophils in regard to chemokines pattern found (Fig. 5D). Neutrophils were abundantly detected in both R1 and C1 segments with a peak reached at 3 days after SCI without any differences in term of amount between each segments. The level decreases in time course. However, immunohistochemistry based on anti-neutrophil elastase marker revealed that the shape of the cells is different in control and after SCI (Fig. 7). In controls, neutrophils are elongated and bipolar (Fig. 7A). Three days after SCI, cells start to make some ramifications and 7 days more cells have ramifications (Fig. 7A and 7C). Ten days later, the num-

ber of cells decreased, but the ones present are still ramified (data not shown). Analyses performed at the level of the blood vessel confirmed that lot of neutrophils are present 3 days (Fig. 7D) after SCI and less at 7 days. At higher magnification, we could discriminate sign of neutrophils extravasation, mimicking movement of cells out of blood vessels toward the injury (Fig. 7E). In comparison, Tregs are present 3 days after SCI, in rostral segment in higher amount than in caudal one. Their levels peak at 7 days for both segments and then decrease at 10 days (Fig. 7E). These results are in line with the cytokine phenotype expressed by the cells (IL6 and CCL20) (Fig. 5). At 3 days after SCI, Tregs presented ramifications (Fig. 7F) whereas at 7 and 10 days, they become round (data not shown). These data are clearly in line with the cytokines pattern observed in Fig. 5 where chemoattractant factors for

TABLE VI

Label free quantification (Intensity-based absolute quantification (IBAQ) value) of identified protein per segments and taking into account time after SCI. the iBAQ values calculated by MaxQuant are proportional to the molar quantities of the proteins

	Ctrl R3	Ctrl R2	Ctrl R1	Ctrl L	Ctrl C1	Ctrl C2	Ctrl C3	3D R3	3D R2	3D R1	3D L	3D C1	3D C2	3D C3	7D R3	7D R2	7D R1	7D L	7D C1	7D C2	7D C3	10D R3	10D R2	10D R1	10D L	10D C1	10D C2	10D C3
axon guidance and neuroprotection	Ctrl R3	Ctrl R2	Ctrl R1	Ctrl L	Ctrl C1	Ctrl C2	Ctrl C3	3D R3	3D R2	3D R1	3D L	3D C1	3D C2	3D C3	7D R3	7D R2	7D R1	7D L	7D C1	7D C2	7D C3	10D R3	10D R2	10D R1	10D L	10D C1	10D C2	10D C3
Mapt	24.071	23.774	23.663	24	24.385	24.683	23.881	23.83	24.2	23.36	23	24.02	24.57	24.62	21.58	24.07	24.49	23	24.78	24.53	24.86	24.873	23.906	24.093	23.2	23.627	24.316	25.207
Ncam1	24.884	24.954	25.271	24.7	25.305	25.524	25.429	24.49	24.99	24.94	23	24.82	25.87	25.71	22.75	25.04	25.34	24	25.48	25.79	25.6	25.279	25.216	25.246	23.8	24.917	25.357	26
Pak1	18.572	19.306	18.409	18.6	18.224	19.786	18.038	18.62	19.42	18.57	19	19.12	19.51	19.24	18.58	19.76	18.69	20	19.25	21.06	19.12	21.66	19.942	18.634	20.1	17.912	18.975	21.054
Pak2	21.416	20.784	21.107	20.5	21.044	21.795	20.854	18.69	21.32	21.52	22	22.91	21.05	20.67	18.54	20.83	21.27	24	24.5	21.44	20.44	22.123	21.674	20.975	22.6	20.782	20.783	21.415
Rac1	24.426	24.091	24.226	23.4	24.069	23.959	23.883	22.89	23.77	23.61	22	23.91	23.4	23.22	21.34	23.72	23.47	24	24.5	23.85	23.19	24.229	24.202	24.181	24.6	24.01	23.793	22.957
Stim1	20.989	20.321	20.547	19.9	19.979	20.475	20.151	20.62	20.98	20.59	20	20.39	20.48	20.20	19.53	20.56	20.69	21	20.78	20.73	20.21	21.478	20.761	20.882	20.2	19.966	20.792	19.852
Stim2	26.147	25.814	26.19	25.6	25.798	25.229	24.16	24.51	24.89	25.06	25	24.91	23.51	24.19	23.19	24.92	24.42	24	24.79	24.76	24.81	24.492	24.455	24.248	23.7	24.447	24.386	23.538
Sema7a	21.342	21.677	20.809	21.1	21.398	20.822	19.959	21.83	21.34	20.6	24	23.32	22.65	22.01	21.54	22.71	21.71	25	22.97	22.41	21.7	21.593	22.255	23.4	24.8	24.523	22.51	21.106
Dcrl1	20.791	19.562	19.281	18.2	20.218	20.151	20.924	20.51	21.34	20.6	20	20.23	21.08	21.77	18.48	20.52	21.04	21	20.93	20.71	21.41	20.942	21.45	21.155	19.6	20.244	20.486	21.105
Nefl	27.669	27.083	26.668	26.4	26.895	27.609	27.016	29.05	28.8	28.03	27	27.8	28.94	28.95	27.11	29.37	28.36	27	28.53	29.12	28.6	29.237	29.445	28.962	27.5	28.01	28.933	28.73
Tardp	22.595	22.756	20.818	20.6	19.873	21.628	19.998	21.62	22.15	22.85	22	21.44	22.81	21.95	19.4	21.33	22.08	22	20.07	21.54	21.26	21.036	21.549	20.709	21	20.148	20.309	21.605
Nlsc	23.506	23.886	23.845	23.6	23.592	23.411	23.193	23.79	24.1	23.43	22	23.4	23.95	24.49	21.8	23.93	23.84	22	23.4	23.92	24.64	24.72	24.178	23.504	22.2	23.252	24.23	24.334
Nim	23.428	22.706	21.857	22.6	23.166	23.185	23.864	23.09	23.68	22.5	22	22.34	23.47	24.36	21.8	22.92	23.51	21	24.02	23.95	24.21	23.433	22.883	22.407	21.5	22.77	24.002	24.083
synapse	Ctrl R3	Ctrl R2	Ctrl R1	Ctrl L	Ctrl C1	Ctrl C2	Ctrl C3	3D R3	3D R2	3D R1	3D L	3D C1	3D C2	3D C3	7D R3	7D R2	7D R1	7D L	7D C1	7D C2	7D C3	10D R3	10D R2	10D R1	10D L	10D C1	10D C2	10D C3
Amph	23.802	23.871	23.676	23.6	23.312	23.779	23.597	23.07	23.34	23.21	21	22.67	23.63	23.74	21.42	23	23.18	22	23.59	23.58	23.64	24.114	23.593	23.232	22.3	22.559	23.481	24.056
Gap43	23.59	22.181	23.677	23.7	22.953	24.014	23.485	23.44	23.33	23.3	22	23.24	23.5	23.27	20.66	23.02	24.17	24	23.93	23.99	23.56	25.308	24.599	23.979	24.4	23.276	24.411	24.397
Septin-11	22.388	23.226	22.213	23	23.306	22.065	22.969	21.99	23.84	21.92	21	22.92	22.3	23.27	19.92	22.28	23.4	22	22.33	22.21	22.49	22.196	22.067	22.83	23	23.053	22.076	22.441
Septin-2	22.236	23.062	22.344	21.4	20.608	20.857	20.908	20.95	21.28	23.05	20	22.36	21.01	20.62	19.09	22.38	23.08	23	22.05	21.06	21.77	20.441	21.635	22.092	22.7	20.778	21.853	21.411
Septin-7	23.047	22.665	22.783	22.4	22.675	22.482	22.761	23.34	22.9	23.49	22	22.59	23.1	23.73	21.6	22.55	23.01	23	22.49	22.65	23.06	22.481	22.757	23.063	22.9	22.5	22.711	23.171
Snap25	23.994	23.456	23.055	23.1	23.046	23.579	23.442	23.56	23.76	22.99	22	23.16	23.48	24.27	20.85	22.99	22.56	22	22.46	23.8	23.9	24.498	23.023	22.962	22.7	22.021	23.671	24.614
Snap91	23.612	22.993	21.998	20.9	22.027	22.583	21.365	23.17	23.03	22.53	22	22.73	23.3	23.47	20.78	22.03	23	23	23.15	23.51	23.12	22.984	22.615	22.772	22.8	22.482	22.648	22.855
Syntaxin-12	22.711	22.752	21.811	22.1	22.027	22.583	21.365	23.17	23.03	22.53	22	22.73	23.3	23.47	20.78	22.03	23	23	23.15	23.51	23.12	22.984	22.615	22.772	22.8	22.482	22.648	22.855
Stx1b	24.604	23.964	24.258	22.5	23.595	23.935	25.325	25.65	24.74	23.98	25	25.19	25.64	25.77	23.08	24.28	24.51	26	24.97	25.04	25.41	25.51	25.392	25.285	25.4	25.033	25.061	25.61
Vcp	25.271	24.623	24.626	24.3	24.623	24.75	24.575	25.42	24.74	25.14	25	25.19	25.64	25.77	23.08	24.28	24.51	26	24.97	25.04	25.41	25.51	25.392	25.285	25.4	25.033	25.061	25.61
Sytn1	23.019	21.549	20.571	18.8	19.456	21.34	22.161	23.52	22.43	21.27	18	21.25	23.41	23.2	21.61	22.16	20.48	18	20.38	22.44	22.85	23.834	22.073	21.792	18.5	19.767	22.289	23.164
Sytn1	22.655	21.502	20.194	19.3	20.817	21.313	21.212	21.16	21.5	21.43	20	21.32	22.58	22.55	19.59	20.35	21.11	20	20.58	22.16	21.78	23.492	22.208	21.482	20.9	20.82	22.158	21.967
Ncdn	23.403	22.168	22.228	22	22.102	23.764	22.164	22.29	22.7	22.85	21	22.89	23.03	23.05	21.61	22.13	21.11	21	22.13	22.37	23.17	23.049	23.283	21.968	20.6	22.524	23.316	23.229
Pdpc	23.284	22.675	22.385	22.3	23.610	23.564	23.867	24	23.28	21.18	21	22.87	23.39	24.02	20.47	22.75	22.03	21	22.93	23.28	24.13	24.338	22.193	21.31	20.1	22.575	23.416	23.94
Nlsc	23.506	23.886	23.845	23.6	23.592	23.411	23.193	23.79	24.1	23.43	23	23.4	23.95	24.49	21.8	23.93	23.84	22	23.4	23.92	24.64	24.72	24.178	23.504	22.2	23.252	24.23	24.334
neuron degeneration	Ctrl R3	Ctrl R2	Ctrl R1	Ctrl L	Ctrl C1	Ctrl C2	Ctrl C3	3D R3	3D R2	3D R1	3D L	3D C1	3D C2	3D C3	7D R3	7D R2	7D R1	7D L	7D C1	7D C2	7D C3	10D R3	10D R2	10D R1	10D L	10D C1	10D C2	10D C3
Sod1	29.133	29.364	28.762	28	29.19	28.804	27.946	29.91	29.76	29.14	29	29.18	29.59	29.56	27.34	29.15	29.48	29	29.84	29.81	29.78	29.834	29.74	29.661	28.9	28.957	29.567	29.915
Vapb	23.805	24.839	23.653	23.1	24.127	23.884	23.109	23.35	24.28	24.12	22	23.03	23.84	24.1	20.7	24.42	23.45	23	24.03	24.54	24.17	24.707	24.793	24.307	23.6	24.423	25.209	25.027
Dcrl1	20.791	19.562	19.281	18.2	20.218	20.151	20.924	20.51	21.34	20.6	20	20.23	21.08	21.77	18.48	20.52	21.04	21	20.03	20.71	21.41	20.942	21.25	21.155	19.6	20.244	20.486	21.106
immune response	Ctrl R3	Ctrl R2	Ctrl R1	Ctrl L	Ctrl C1	Ctrl C2	Ctrl C3	3D R3	3D R2	3D R1	3D L	3D C1	3D C2	3D C3	7D R3	7D R2	7D R1	7D L	7D C1	7D C2	7D C3	10D R3	10D R2	10D R1	10D L	10D C1	10D C2	10D C3
Igal3	22.834	25.013	26.395	24.9	25.515	23.072	17.279	27.03	28.23	29.71	29	29.15	28.01	24.88	24.5	28.22	29.24	30	28.41	27.94	24.65	26.642	28.377	29.498	30.7	27.971	26.742	24.825
Igal1	27.758	27.96	27.995	27.3	27.546	27.072	26.936	28.08	28.68	28.66	28	28.23	28.41	28.16	26.34	29.16	29.41	29	29.38	29.35	28.45	28.445	29.217	29.476	29.3	28.583	28.947	



FIG. 5. Chemokines and cytokines array after SCI in CM from R1 and C1 for control and 3, 7, and 10 days post injury. The rat cytokine array assay was performed in SC conditioned media. Blue bars show R1 CM, and orange indicates C1 CM. The bar diagrams represent the ratio of the spot mean pixel densities/reference point pixel densities. A, Comparison of cytokines and chemokines secretion in R1 segment at 3, 7 and 10 days after SCI and control. B, Comparison of cytokines and chemokines secretion in C1 segment at 3, 7, and 10 days after SCI and control. Significant differences were analyzed using Student's *t* test **p* < 0.05, ***p* < 0.01, ****p* < 0.001. Quantification of immune cells recruitment in control and 3, 7, and 10 days post-injury, comparison between R1 rostral and C1 caudal segments. C, Number of Iba1 positive microglia recruited in gray and white matters. D, Percentage of neutrophil elastase-positive neutrophils and E, FoxP3-positive Tregulators recruited in white matter. **p* < 0.05, ***p* < 0.001, ****p* < 0.0001 One-way ANOVA.

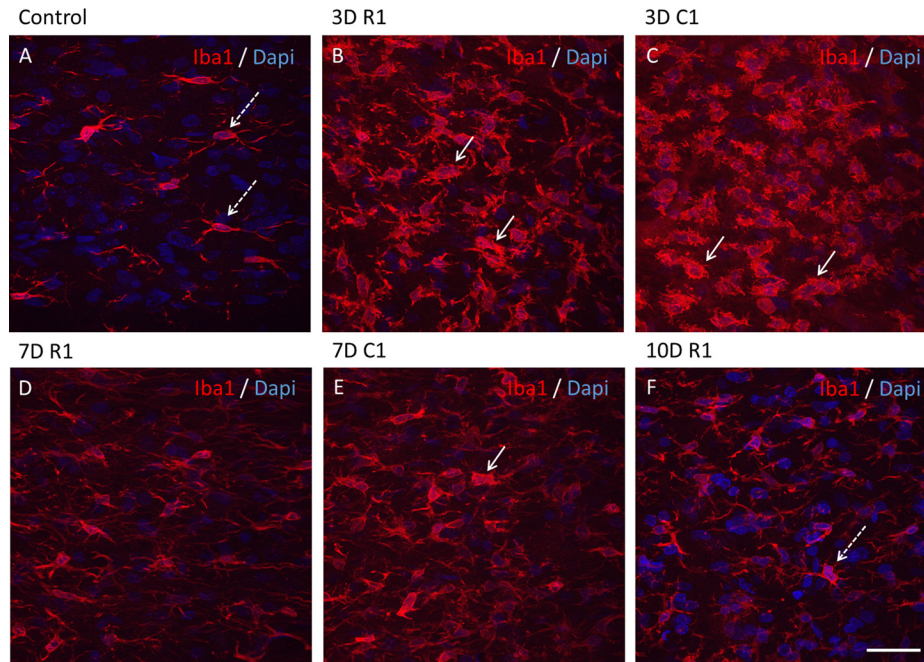


FIG. 6. Representative longitudinal sections of spinal cord revealing Iba1 microglia positive cells rostrally (B, D, E) and caudally (C, F) to the lesion site after SCI (3D, 7D, 10D) in comparison to control (A). Note, activated microglia with hypertrophied cell body and retracted processes at 3 and 7 days at C1 segment (B, C, E arrows-full) in comparison to resting microglia in control (A, arrows-intermittent) or mild activation, re-appearing fine ramification at 10D (F). Scale bar = 25 μm .

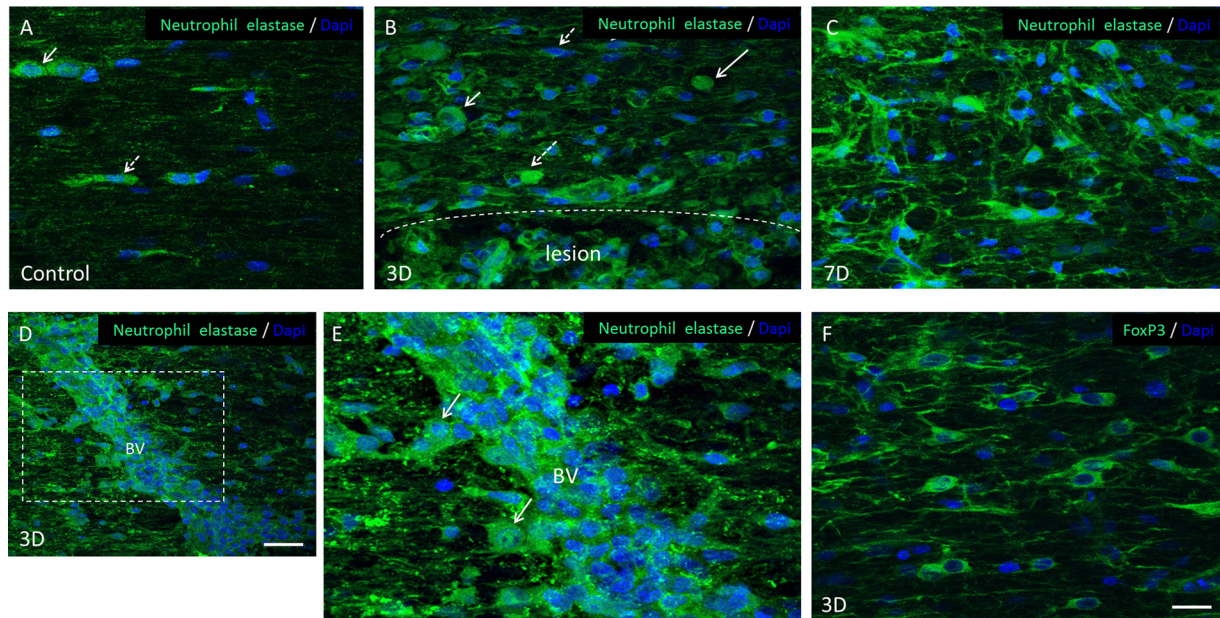


FIG. 7. Fluorescent immunohistochemistry performed on control spinal cord sections and after SCI (3 and 7 days) analyze for neutrophils with neutrophil elastase antibody and lymphocytes Tregulator with FoxP3 antibody. Infiltrated neutrophils showed either elongated (arrow- intermittent) or round shape morphology (arrow-full) at 3 days after SCI (B), whereas at 7 days cellular ramification was apparent in most neutrophils (C). Many blood vessels close to the injury site were filled with neutrophils at 3 and 7 days after SCI (D). At higher magnification, neutrophils extravasation, mimicking movement of cells out of blood vessels toward the injury can be detected (E). Scale bar A-F = 20 μm , D = 40 μm , E = 15 μm . (C3>C2>C1) for control, 3 days, 7 days, and 10 days.

neutrophils and microglia are detected. Neutrophils and microglia are recruited between 0 and 3 days after SCI in caudal segments and their levels decrease at 7 days. Similarly, Tregs

are recruited between 3 and 7 days and peak at 7 days. These data are in line with the presence of CXCL1, CXCL3, CXCL5, CCL20, TIMP-1, and IL6 in R1, at 3 days, which are known to

attract neutrophils and lymphocytes. In C1, a delay is observed for the recruitment of the Tregs, which are recruited 7 days after SCI which correlate with the detection of CCL20 in C1 only at 7 days, whereas neutrophils and microglial cells are already present at 3 days. Taken together the results showed that C1 is clearly different from R1 in term of cell types, molecular content in time course and revealed to be a target segment for therapy.

Focus on C1 Biomarkers for a Targeted Treatment—Because of the presence of neurofascin and MEMO 1 as specific markers of C1 in time course, we investigated the role of these proteins in SCI. Neurofascin could serve as autoantigen. Indeed, in patients sera suffering from inflammatory demyelinating polyneuropathy or multifocal motor neuropathy, specific autoantigens including neurofascin have been found⁶. Moreover, emerging data indicate that pathological sequelae that accompany central nervous system trauma, e.g. SCI, have characteristics of a self-directed immunological disease. Autoantibodies could exacerbate tissue damage impairing neurological recovery and amplify SCI injury. Moreover, the label free quantification (Intensity-based absolute quantification value) of identified protein per segments and taking into account time after SCI have revealed the presence of immunoglobulin (IgG2a) in lesion 3 days after SCI (Table VI). The fact that such cytotoxic immunoglobulin was detected so early after SCI is not in line with a classical adaptive response. In this context, we focused on tracking the occurrence of autoantibodies in time course after SCI. We performed double labeled immunofluorescence on frozen longitudinal sections after 3, 7, and 10 days post-SCI to establish the cell types (neurons, astrocytes and microglia) expressing IgGs. In spinal cord tissue, at 3 days postinjury, IgG-immunoreactivity using both antibodies was found in most neurons (labeled with anti-NeuN), with higher prevalence throughout the layers LV-LIX (Fig. 8A). However, in the case of motor neurons, we could see differences in the double staining expression (Fig. 8A). These IgGs have been characterized (Fig. 8B). In fact, the conditioned media collected at 3, 7, and 10 days post-SCI were incubated with protein A and afterward eluted proteins were separated on SDS-PAGE (Fig. 8B). After silver staining, clear bands are retrieved from the gel at 3 days, but not at 7 or 10 days after SCI. Each selected bands at 25 kDa, 55 kDa, and 75 kDa have been digested in gel before subjected to shot-gun analysis. The identification, performed by MS/MS, of the proteins confirms the presence of the IgGs kappa-chain VJC precursor of fragment (166–218) (Fig. 8B).

Orthogonal views confirmed that anti-IgG (green) and anti-NeuN (red) staining overlap in some, but not all motor neurons (Fig. 8). Thus, some neurons diffusely stained with anti-NeuN were also heavily positive for IgG (Fig. 8C), whereas other neurons were lacking anti-IgG positivity completely, or exhibited labeling only on their surface membrane (Fig. 8D). In few cases we could distinguish also IgG-positive nerve pro-

cesses. Similarly as in neurons, a double anti-GFAP and anti-IgG labeling confirmed positivity in astrocytes (Figs. 9D–9F). Many GFAP-positive astrocytes with hypertrophic appearance and thick processes indicating activated phenotype co-expressed IgG (yellow) primarily at the injury site. These reactive IgG-positive astrocytes were found around neuronal bodies and vessels (Figs. 9D–9F). Baseline expression of GFAP-positive astrocytes with the characteristic round small soma and slender, long processes, but lacking IgG-expression were seen in control spinal cord distributed throughout white and gray matters (Figs. 9A–9C) as well as in the regions out from injury site (Fig. 9G). Furthermore, no GFAP-positive astrocytes expressing IgG were detected in the spinal cord tissue from 7 days and 10 days after SCI. Interestingly, microglia did not express IgG in any of studied groups (data not shown). In addition, to exclude possible effect of B-cells mediated IgG production, we evaluated spinal cord tissue containing multiple *in vivo* injections of rabbit anti-rat CD-20 antibody. In this context, 1 h after SCI, 3 intraspinal injections per animal were applied bilaterally to the lesion site, at the level of the lesion cavity and at rostral and caudal segments. Basso, Beattie and Bresnahan studies at 0, 1, 3, 7, 14, 21 days until 28 days after SCI did not reveal any improvement compared with SCI without anti-CD20 treatment (Fig. 10). In sagittal sections double labeled with primary goat anti-rat IgG2a and mouse anti-NeuN, we did not observe significant attenuation of neurons expressing IgG. The injection tract was occupied with small amount of erythrocytes that were surrounded by neurons with intensely labeled IgGs as well as those farther from injection (Fig. 9H).

DISCUSSION

We have previously investigated the spectrum of released molecules in the conditioned media (CM) from the spinal cord central lesion and adjacent rostral and caudal segments at 3 days after spinal cord injury (SCI) in order to specify the molecular environment within the proximity of the injured tissue. Data suggested that regionalization in terms of inflammatory and neurotrophic responses may occur between rostral and caudal segments in acute SCI. Here, we extended our investigation both spatially and temporally using cellular, biochemical and proteomics techniques. We have shown that the lesion segment is the most divergent from the others ones and is mostly implicated in acute immune response through microglia and neutrophils activation, oxidative stress and lipid peroxidation. R1 and C1 segments present markers for inflammation, axonal regeneration, demyelination and even neurite inhibitors factors. By contrast, segments R3 and C3 and R2 and C2 expressed neurites outgrowth, cell proliferation, cell differentiation, endocytosis and cytoskeleton organization activated pathways. Moreover, these segments are very close in term of the molecular content in time course after lesion and are mostly divergent from R1 and C1 segments. A deeper analysis based on the differential distribution of the

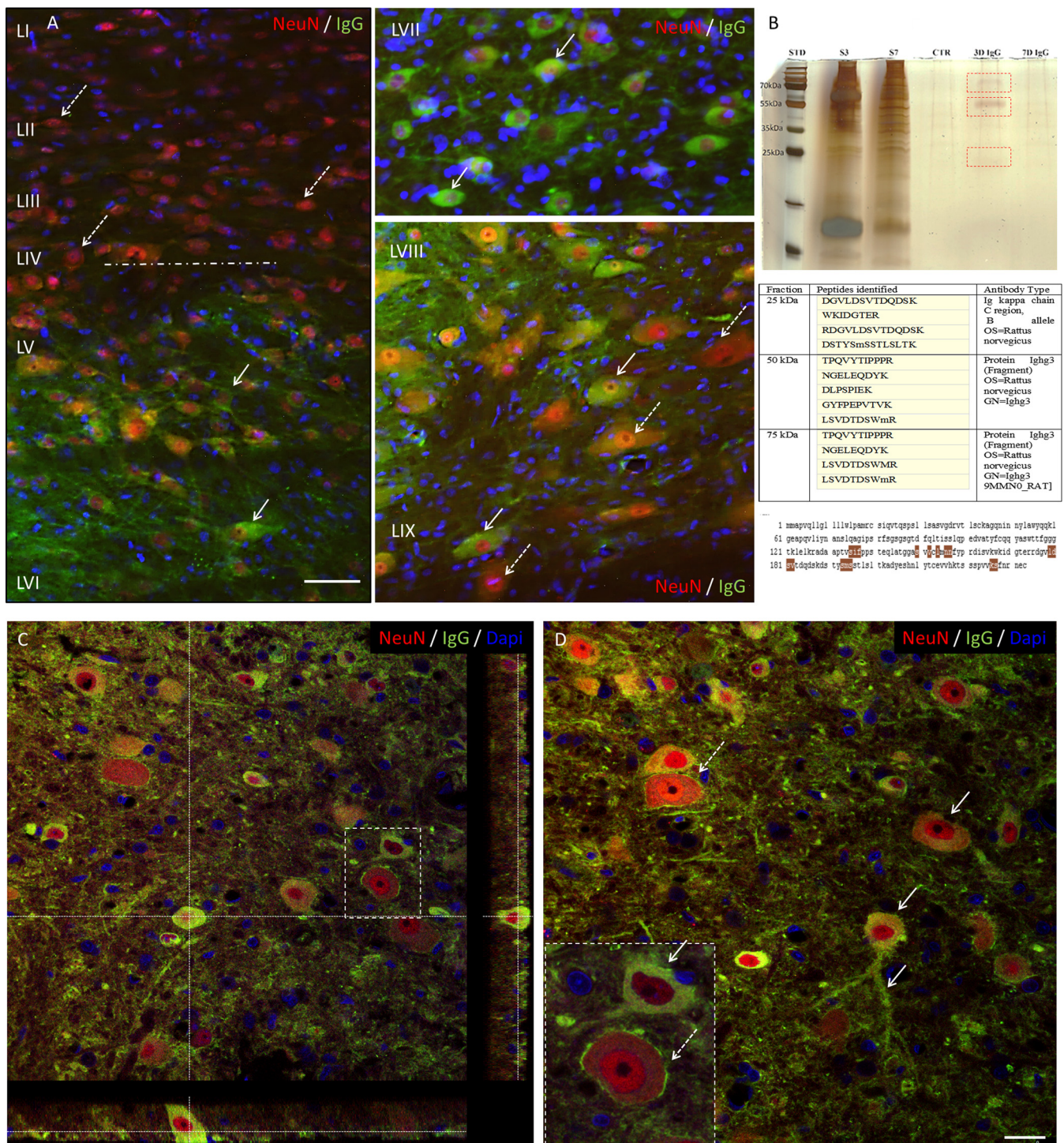


FIG. 8. Specific expression of IgG positivity in neurons through the spinal cord laminae I-IX at 3D. *A*, Double immunofluorescence labeling revealed colocalization of NeuN-positive (red) and IgG-positive (green) cells that were restricted throughout laminae LV-LIX, whereas superficial laminae LI-LIV were IgG-negative. *B*, SDS-PAGE electrophoresis and silver staining confirmed the presence of autoantibodies at 3 days after injury by three bands localized at 70 kDa, 55 kDa and 25 kDa. After in-gel digestion, shot-gun proteomics analysis was performed to confirm the presence of IgGs, for each band (antibody type). BlastP has shown 62% of sequence alignment. Amino acid residues in brown consist of the polypeptide binding sites of the antibody, *i.e.*, sites 135–137, 150, 152, 154, 156–157, 179–182, 193–195, 226–227. Scale bar = 50 μ m. Confocal images demonstrating the presence of IgGs in the spinal cord neurons. *C*, Orthogonal views confirmed that anti-IgG (green) and anti-NeuN (red) stainings overlap in some, but not all motor neurons. *D*, The distribution of IgGs was different across neuronal populations. Although in some neurons intense IgG positivity (green) was homogenously distributed with the cell body and processes (*D*, arrow-full), other neurons exhibited IgG expression limited to their membrane (arrow-intermitted). Scale bar = 25 μ m.

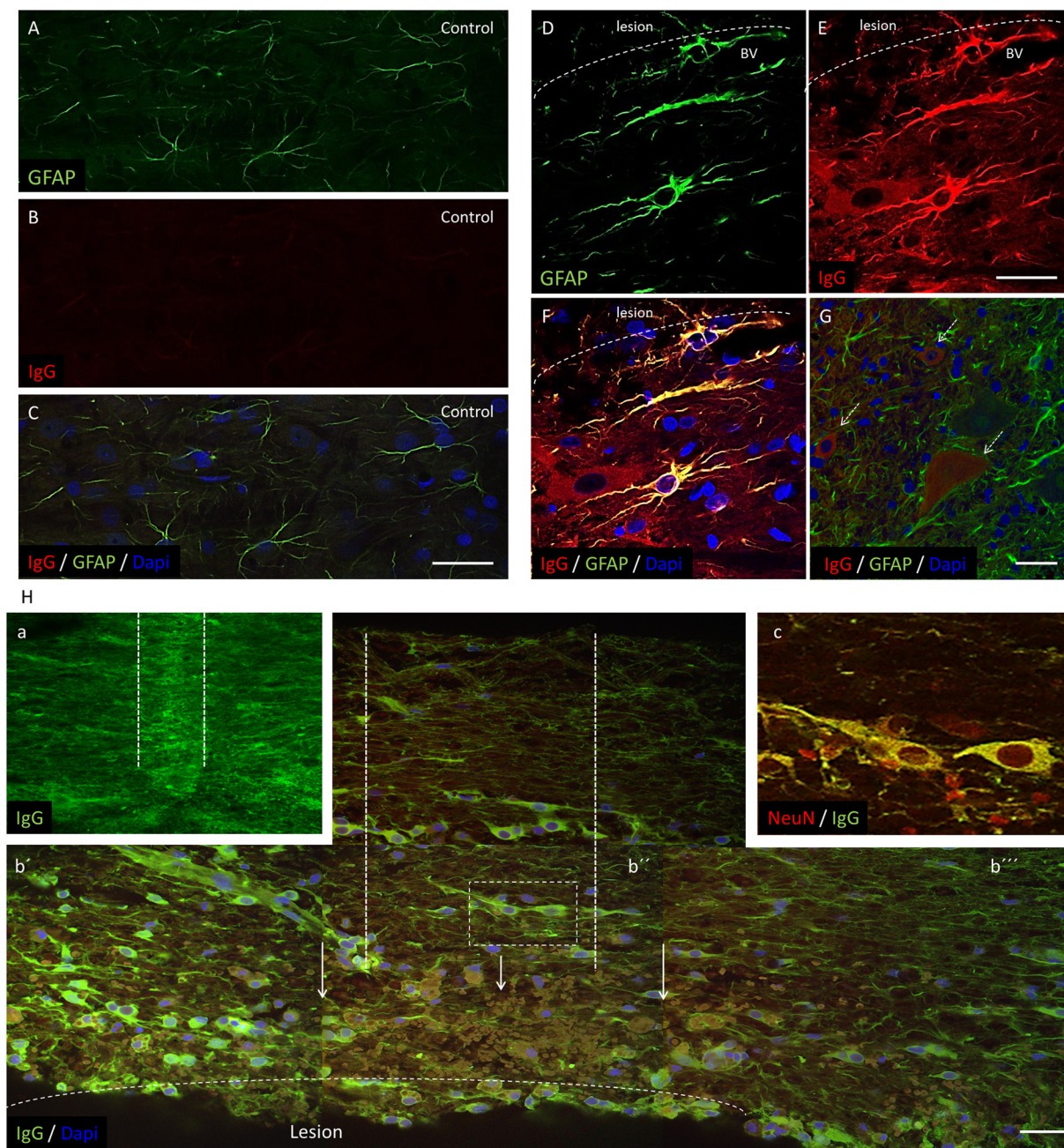


FIG. 9. Representative images of GFAP-positive astrocytes expressing IgG. Control spinal cord sections contained typical astrocytes with star like thin processes (A), lacking IgG (red) expression (B), confirmed by double labeling (C). In contrast, reactive astrocytes with hypertrophic appearance and thick processes, coexpressed IgG (yellow) at the lesion site were found around neuronal bodies and vessels after 3days (D–F). In neighboring rostral and caudal segments, some neurons expressing IgG (red, arrows), but not GFAP-positive astrocytes (green) were detected (G). Scale bar = 25 μm . H) Intraspinal delivery of anti-CD-20 antibody in rats surviving 3days. (a) Identification of anti-CD-20 delivery tract within the spinal cord tissue labeled with goat-anti rat IgG (green). Note, there is no visible depletion of IgG labeling. (b, b', b'') composite of four detailed figures showing the region adjacent to the lesion, where delivery of CD-20 was performed (outlined by two bars) and is accompanied with infiltrated erythrocytes (arrows) and neurons expressing IgG. At the injections site as well in rostro- caudal axis neurons and their processes expressing IgG were detected. (c) Detail of boxed area from b'' shows double labeling of anti-IgG and anti NeuN confirmed neuronal expression of IgGs. Scale bar = 30 μm .

unique and common/intersected biological and functional pathways among the three spinal cord rostral and caudal regions (C1,C2, C3 versus R1, R2, R3) factored by time of SCI (3, 7, and 10 days) clearly demonstrate that R1 is different

from C1. The Subnetwork Enrichment Analysis (SEA) showed that only 40 specific proteins unique can be retrieved from each segment taking into account the time course and the spatial localization nearby the lesion (Table III). In this context,

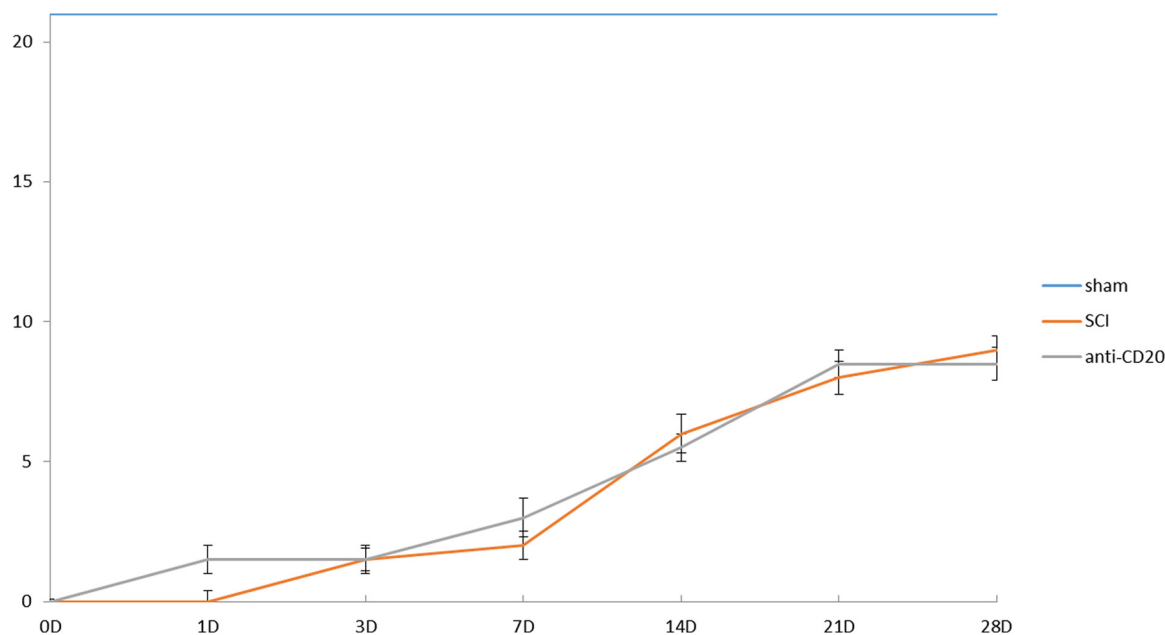


FIG. 10. BBB studies at 0, 1, 3, 7, 10, 14, 21, and 28 days in following experimental groups: in sham, following SCI, and after SCI + anti-CD20 antibody injection. Note, no significant differences in motor function recovery between SCI and SCI+ anti-CD20 treatment during survival.

the chemokine CXCL2 is considered as unique in R1 whereas in C1, the neurofascin and the mediator of cell motility 1 (MEMO 1), which control cell migration by relaying extracellular chemotactic signals to the microtubule cytoskeleton, are detected. The molecular 2D map obtained via MALDI-MSI analysis completed by a lipidomic study in both lesion and C1 (Table V) strengthens these results. The lipid profile detected in lesion is mostly different in term of level of expression to the one detected in C1. The 3D map of the C1 segment at the level of the gray and white matter confirms such differences.

The fine analysis of C1 segments showed, that in time course, C1 segments express neurite inhibitors like MEMO1, neurocan, as well as neurite stimulators such as neurofascin and amphiphysin proteins. MEMO1 is implicated in MEMO1-RHhoA-DIAPH1 signaling pathway which plays an important role in ErbB2-dependence (34). Neurocan is known to inhibit neurites outgrowth (37). After spinal cord injury, neurocan, brevican, and versican expression is increased within days in injured spinal cord parenchyma surrounding the lesion site and peaks at 2 weeks. Neurocan and versican are persistently elevated for 4 weeks post-injury, and brevican expression persisted for at least 2 months (37). On the contrary, neurofascin and amphiphysin, are two proteins known to be implicated in neurites outgrowth, are located at the level of the growth cone. However, these two proteins are also involved in autoimmunity as autoantigens (38–41).

With respect to the proteomic results our next step was to investigate the nature of cellular processes, and identify the cellular content responsible for production of detected molecules. It is well established that injury to the blood-brain barrier facilitates the extravasations of cellular components as

well as immunoglobulins and complement proteins into the neural parenchyma (42, 43). The recruitment of blood-derived cellular components is dependent on inflammatory processes that are orchestrated by secondary damage at the lesion site. Thus, the cytokine environment in the central nervous system (CNS) may determine the phenotype of the inflammatory infiltrate. For example, intra-spinal injections of tumor necrosis factor (TNF)- α induced monocyte infiltration whereas interleukin (IL)-1 β recruited mostly neutrophils (44, 45). Present data confirm that released cytokines and chemokines correlate with the activation of microglia and recruitment of neutrophils in segments anterior and posterior to the lesion site. These cells, along with the soluble mediators/proteins (e.g. cytokines, complement), interact to eliminate pathogenic elements in the affected site, while simultaneously priming the site for repair. Within the spinal cord, microglia are the resident tissue macrophages that primarily control the rate, magnitude and the ultimate fate (supporting regeneration or degeneration) of inflammatory processes at the injury site. However, in our study we have taken into account the cellular microenvironment in which microglia become activated (46). Therefore, we have analyzed response of microglia within the white and gray matters separately in rostro-caudal axis with time.

Present data confirmed striking differences in the number and morphology of microglia cells during injury time. The extent of microglia activation was significantly higher in gray than in white matter tracts in the caudal segments during the time period 3–7 days after injury, whereas at 10 days it dropped down. These discrepancies may be dependent on two factors: i) the metabolic changes in microglial function

that are differentially affected at the gray matter necrotizing injury site and in degenerating white matter tracts, or ii) on the extent of blood-brain barrier injury, which varies between the gray and white matter (42, 47), and on the severity of injury. In this context, gray and white matters microglia express distinct morphologies and levels of cell surface antigens (48, 49), which most likely correspond with unique cell functions (50, 51). Indeed, the microenvironment in which microglia and/or macrophages are activated influences their neurotrophic or neurotoxic effector potential (52, 53) that correspond to M1 and M2 phenotypes. The predominance of microglia activation in caudal segments is in line with our previous and present studies confirming the occurrence of severe inflammation-associated tissue damage taking place in this segment and possibility to switch/or not from M1 to M2 phenotype (29).

In contrast to tissue resident microglia (54), neutrophils are the first inflammatory cells to arrive at the site of injury, with a peak at 24 h post injury. Recruitment of T regulators (Tregs) (Foxp3-positive) firstly occurs at 3 days and mainly at the level of the rostral segment and peaks at 7 days in both rostral and caudal sites. These results are in line with the presence of CCL20 in rostral segment and not in caudal at 3 days and then found at 7 days in both segments. In fact, CCL20 is known to recruit Tregs (55). Presence of recruitment of thymic-derived FoxP3-Tregs was recently suggested (56). Tregs can reduce inflammation and enhance CNS repair (57). Presence of such cells predominantly in rostral segment is in line with the cytokine medium which favor expression of macrophages expressing an M2 phenotype and production of neurotrophic factors (29). Moreover, the time difference of recruitment between rostral and caudal segments of these cells can also contribute to the less enhancement of neurites outgrowth in C1 compared with R1.

Thus, the spinal cord, as a part of CNS has generally been described as having immune privilege, but several facts motivated us to reexamine this principle. Particularly, in a search for presence of antibodies responding to neurofascin found in caudal segment, we have proven via immunohistochemistry that IgGs are expressed by interneurons and motor neurons, 3 days after spinal cord injury suggestive of autoimmunity. Furthermore, in CM from SCI, using biochemical and proteomic analysis, we showed by protein A, gel electrophoresis associated to mass spectrometry analyses, content of spinal IgGs at 3 days, but not at 7 or 10 days after injury. Here, we need to mention few important findings regarding neuronal IgG positivity and IgG sources. Firstly, spinal neurons revealed distinct expression of IgG throughout dorso-ventral axis. Although sensory neurons in laminae I-IV were negative, the neuronal populations corresponding to interneurons and motor neurons of laminae V-IX were most likely positive for IgG, with few discrepancies. The confocal orthogonal views showed that some neurons revealed very clear golgi-like staining of soma and processes, whereas in others the IgG expression was found solely in the neuronal soma, or was

restricted to superficial membrane outlining the neuronal body. We suggest that divergence of neuronal population IgG response may be caused by their different vulnerability to injury or by the extent and severity of impairment *in situ*. Thus, it is more likely that we can see early response of most vulnerable interneurons and motor neurons expressing IgG that are probably behaving to secondary damage processes, similarly as are responding CA1 vulnerable neurons in hippocampus (58). Furthermore, also spinal cord ischemia leads to selective loss of highly vulnerable inhibitory GABAergic interneurons followed by motor neurons resulting to spasticity (59). There are other studies further confirming vulnerability of interneurons, and motor neurons to stress, ischemia, injury or various neurodegenerative diseases. Secondly, it is important to identify the source of IgGs. Because, the motor neurons are projecting outside the CNS, it is assumed that they can take up IgGs from peripheral tissues, by retrograde transport from nerve terminals (60, 61). However, this may not be the case for the interneurons that terminate only within the spinal cord. But, they may have the ability to take up IgGs from the cerebrospinal fluid (CSF) (62).


On other hand, there are studies suggesting productions of IgGs by neurons (63). Present results document specific transient neuronal expression of IgGs, but we do not have proof of their sources, which needs further transcriptomics studies. Another important issue that needs to be mentioned is the functionality of IgGs and their epitopes. There are two contradictory hypotheses that should be taken into account, where IgGs pose as neuroprotective (64) or neurodestructive (60). The first one suggests that neuron-derived IgGs has the ability to protect neurons from early apoptosis and cell death induced by complement. The second one refers to IgGs as detrimental factors of neurons, attacking the regeneration of axons after spinal cord injury (60) (B cells produce pathogenic antibodies and impair recovery after spinal cord injury in mice (65)). Our results are more likely in a favor of the first one, because we identify early, transient expression of IgGs at 3 days. Why we did not see IgGs at 7 or 10 days, we do not have reasonable explanation. Moreover, injection at 1 h after lesion of anti-CD20 did not attenuate the expression of IgGs detected at 3 days post-SCI and Basso, Beattie and Bresnahan motor score of the animals was similar to the one with preliminary treatment. These data tend to reveal that antibodies are not produced by active B cells. Nevertheless, to better understand this interesting finding; we need to follow up with further studies.

Taken together, we described for the first time the molecular and cellular processes occurring after SCI on the temporal and spatial levels. We established that differences in term of molecular pathways occurred between lesion, C1, R1, and the other segments. In fact, R2, C2, and R3, C3 coexpressed the molecules implicated in same physiological pathways. Only 40 specific proteins for each segment and taking into account time after injury have been characterized. Except the

lesion, C1 is the most divergent. The presence of neurites outgrowth inhibitors in C1, with a delay in recruitment of Tregs, favors the lack of regeneration process in C1. Moreover, the presence of IgGs at the lesion site, at 3 days post-SCI, can also be one of the factors that contribute to limitation of the regeneration process. However, treatment of anti-CD20 did not showed any impact *in vivo* in IgGs presence and in enhancement of locomotor function. These results open the door to a novel view of the SCI treatment by considering the C1 as the therapeutic target in order to modulate inflammation and stimulate regeneration process.

* This research was supported by a collaboration between the Fundamental and Applied Biology Mass Spectrometry Laboratory (MS) and grants from Ministère de L'Éducation Nationale, L'Enseignement Supérieur et de la Recherche, INSERM ,Région Nord-Pas de Calais (to S.D.), SIRIC ONCOLille Grant INCa-DGOS-Inserm 6041aa (IF) and Université de Lille 1 (S.D.), VEGA 2/0125/15 (DC), APVV SK-FR-2015-0018 (DC), Stefanic 2016 (MS) and APVV 0472-11 (DC).

 This article contains supplemental material.

 To whom correspondence should be addressed: University of Lille, INSERM, U1192 - Laboratoire Protéomique, Réponse Inflammatoire et Spectrométrie de Masse-PRISM, F-59000 Lille, France Tel.: +33-320-4194; Fax: +33-320-4354; E-mail: Michel.salzet@univ-lille1.fr.

^a Co-author: The authors declare no competing financial interests.

REFERENCES

- Beattie, M. S., Hermann, G. E., Rogers, R. C., and Bresnahan, J. C. (2002) Cell death in models of spinal cord injury. *Prog. Brain Res.* **137**, 37–47
- Tator, C. H. (1995) Update on the pathophysiology and pathology of acute spinal cord injury. *Brain Pathol.* **5**, 407–413
- Schwab, M. E., and Bartholdi, D. (1996) Degeneration and regeneration of axons in the lesioned spinal cord. *Physiol. Rev.* **76**, 319–370
- Schwab, M. E., and Bartholdi, D. (1996) Degeneration and regeneration of axons in the lesioned spinal cord. *Physiol. Rev.* **76**, 319–370
- Rosignol, S., Schwab, M., Schwart, M., and Fehlings, M. G. (2007) Spinal cord injury: time to move? *J. Neurosci.* **27**, 11782–11792
- Leybold, B. G., Flanders, A. E., Schwartz, E. D., and Burns, A. S. (2007) The impact of methylprednisolone on lesion severity following spinal cord injury. *Spine* **32**, 373–378; discussion 379–381
- Rowland, J. W., Hawryluk, G. W., Kwon, B., and Fehlings, M. G. (2008) Current status of acute spinal cord injury pathophysiology and emerging therapies: promise on the horizon. *Neurosurg Focus* **25**, E2
- Hawryluk, G. W., Rowland, J., Kwon, B. K., and Fehlings, M. G. (2008) Protection and repair of the injured spinal cord: a review of completed, ongoing, and planned clinical trials for acute spinal cord injury. *Neurosurg Focus* **25**, E14
- Wells, J. E., Hurlbert, R. J., Fehlings, M. G., and Yong, V. W. (2003) Neuroprotection by minocycline facilitates significant recovery from spinal cord injury in mice. *Brain* **126**, 1628–1637
- Huang, H., Fan, S., Ji, X., Zhang, Y., Bao, F., and Zhang, G. (2009) Recombinant human erythropoietin protects against experimental spinal cord trauma injury by regulating expression of the proteins MKP-1 and p-ERK. *J. Int. Med. Res.* **37**, 511–519
- Bradbury, E. J., Moon, L. D., Popat, R. J., King, V. R., Bennett, G. S., Patel, P. N., Fawcett, J. W., and McMahon, S. B. (2002) Chondroitinase ABC promotes functional recovery after spinal cord injury. *Nature* **416**, 636–640
- Schwab, M. E. (2004) Nogo and axon regeneration. *Curr. Opin. Neurobiol.* **14**, 118–124
- Schwab, M. E. (2002) Repairing the injured spinal cord. *Science* **295**, 1029–1031
- Fehlings, M. G., and Vawda, R. (2011) Cellular treatments for spinal cord injury: the time is right for clinical trials. *Neurotherapeutics* **8**, 704–720
- Vanicky, I., Urdzikova, L., Saganova, K., Cizkova, D., and Galik, J. (2001) A simple and reproducible model of spinal cord injury induced by epidural balloon inflation in the rat. *J. Neurotrauma* **18**, 1399–1407
- Grulova, I., Slovinska, L., Blasko, J., Devaux, S., Wisztorski, M., Salzet, M., Fournier, I., Kryukov, O., Cohen, S., and Cizkova, D. (2015) Delivery of Alginate Scaffold Releasing Two Trophic Factors for Spinal Cord Injury Repair. *Sci. Reports* **5**, 13702
- Cox, J., and Mann, M. (2008) MaxQuant enables high peptide identification rates, individualized p.p.b.-range mass accuracies and proteome-wide protein quantification. *Nat. Biotechnol.* **26**, 1367–1372
- Cox, J., Neuhauser, N., Michalski, A., Scheltema, R. A., Olsen, J. V., and Mann, M. (2011) Andromeda: a peptide search engine integrated into the MaxQuant environment. *J. Proteome Res.* **10**, 1794–1805
- UniProt, C. (2012) Reorganizing the protein space at the Universal Protein Resource (UniProt). *Nucleic Acids Res.* **40**, D71–D75
- Cox, J., Hein, M. Y., Luber, C. A., Paron, I., Nagaraj, N., and Mann, M. (2014) Accurate proteome-wide label-free quantification by delayed normalization and maximal peptide ratio extraction, termed MaxLFQ. *Mol. Cell Proteomics* **13**, 2513–2526
- Vizcaino, J. A., Deutsch, E. W., Wang, R., Csordas, A., Reisinger, F., Rios, D., Dianes, J. A., Sun, Z., Farrah, T., Bandeira, N., Binz, P. A., Xenarios, I., Eisenacher, M., Mayer, G., Gatto, L., Campos, A., Chalkley, R. J., Kraus, H. J., Albar, J. P., Martinez-Bartolome, S., Apweiler, R., Omenn, G. S., Martens, L., Jones, A. R., and Hermjakob, H. (2014) ProteomeX-change provides globally coordinated proteomics data submission and dissemination. *Nat. Biotechnol.* **32**, 223–226
- Vizcaino, J. A., Cote, R. G., Csordas, A., Dianes, J. A., Fabregat, A., Foster, J. M., Griss, J., Alpi, E., Birim, M., Contell, J., O'Kelly, G., Schoenegger, A., Ovelleiro, D., Perez-Riverol, Y., Reisinger, F., Rios, D., Wang, R., and Hermjakob, H. (2013) The PRoteomics IDentifications (PRIDE) database and associated tools: status in 2013. *Nucleic Acids Res.* **41**, D1063–1069
- Montejo, J., Zuberi, K., Rodriguez, H., Bader, G. D., and Morris, Q. (2014) GeneMANIA: Fast gene network construction and function prediction for Cytoscape. *F1000Res* **3**, 153
- Chen, E. Y., Tan, C. M., Kou, Y., Duan, Q., Wang, Z., Meirelles, G. V., Clark, N. R., and Ma'ayan, A. (2013) Enrichr: interactive and collaborative HTML5 gene list enrichment analysis tool. *BMC Bioinformatics* **14**, 128
- Yuryev, A., Kotelnikova, E., and Daraselia, N. (2009) Ariadne's ChemEffect and Pathway Studio knowledge base. *Expert Opin. Drug Discov.* **4**, 1307–1318
- Bonnet, A., Lagarrigue, S., Liaubet, L., Robert-Granie, C., Sancristobal, M., and Tosser-Klopp, G. (2009) Pathway results from the chicken data set using GOTM, Pathway Studio and Ingenuity softwares. *BMC Proc.* **3**, S11
- Pyatnitskiy, M., Mazo, I., Shkrob, M., Schwartz, E., and Kotelnikova, E. (2014) Clustering gene expression regulators: new approach to disease subtyping. *PLoS ONE* **9**, e84955
- Daraselia, N., Wang, Y., Budoff, A., Lituev, A., Potapova, O., Vansant, G., Monforte, J., Mazo, I., and Ossovskaya, V. S. (2012) Molecular signature and pathway analysis of human primary squamous and adenocarcinoma lung cancers. *Am. J. Cancer Res.* **2**, 93–103
- Cizkova, D., Le Marrec-Croq, F., Franck, J., Slovinska, L., Grulova, I., Devaux, S., Lefebvre, C., Fournier, I., and Salzet, M. (2014) Alterations of protein composition along the rostro-caudal axis after spinal cord injury: proteomic, *in vitro* and *in vivo* analyses. *Front. Cell Neurosci.* **8**, 105
- Thiele, H., Heldmann, S., Trede, D., Strehlow, J., Wirtz, S., Dreher, W., Berger, J., Oetjen, J., Kobarg, J. H., Fischer, B., and Maass, P. (2014) 2D and 3D MALDI-imaging: conceptual strategies for visualization and data mining. *Biochim. Biophys. Acta* **1844**, 117–137
- Bonnel, D., Longuespee, R., Franck, J., Roudbaraki, M., Gosset, P., Day, R., Salzet, M., Fournier, I. (2011) Multivariate analyses for biomarkers hunting and validation through on-tissue bottom-up or in-source decay in MALDI-MSI: application to prostate cancer. *Anal Bioanal Chem.* **401**(1), 149–165
- Chambolle, A. (2004) An algorithm for total variation minimization and applications. *J. Mathematical Imaging Vision* **20**, 89–97
- Zhang, J., Li, D., Hu, W., Chen, Z., and Yuan, Y. (2014) Multilabel image annotation based on double-layer PLSA model. *ScientificWorldJournal* **2014**, 494387
- Zaoui, K., Honore, S., Isnardon, D., Braguer, D., and Badache, A. (2008) Memo-RhoA-mDia1 signaling controls microtubules, the actin network, and adhesion site formation in migrating cells. *J. Cell Biol.* **183**, 401–408

35. Mathey, E. K., Derfuss, T., Storch, M. K., Williams, K. R., Hales, K., Woolley, D. R., Al-Hayani, A., Davies, S. N., Rasband, M. N., Olsson, T., Moldenhauer, A., Velhin, S., Hohlfeld, R., Meinel, E., and Linington, C. (2007) Neurofascin as a novel target for autoantibody-mediated axonal injury. *J. Exp. Med.* **204**, 2363–2372
36. Han, G., Wu, D., Yang, Y., Li, Z., Zhang, J., and Li, C. (2015) CrkL mediates CCL20/CCR6-induced EMT in gastric cancer. *Cytokine* **76**, 163–169
37. Jones, L. L., Margolis, R. U., and Tuszynski, M. H. (2003) The chondroitin sulfate proteoglycans neurocan, brevican, phosphacan, and versican are differentially regulated following spinal cord injury. *Exp. Neurol.* **182**, 399–411
38. Neshige, S., Hara, N., Takeshima, S., Iwaki, H., Shimoe, Y., Takamatsu, K., and Kuriyama, M. (2014) Anti-amphiphysin antibody-positive paraneoplastic neurological syndrome with a longitudinally extensive spinal cord lesion of the dorsal column. *Clin. Neurol.* **54**, 572–576
39. Levin, M. C., Lee, S., Gardner, L. A., Shin, Y., Douglas, J. N., and Cooper, C. (2013) Autoantibodies to non-myelin antigens as contributors to the pathogenesis of multiple sclerosis. *J. Clin. Cell. Immunol.* **213**, 4–10
40. Huijbers, M. G., Querol, L. A., Niks, E. H., Plomp, J. J., van der Maarel, S. M., Graus, F., Dalmau, J., Illa, I., and Verschuuren, J. J. (2015) The expanding field of IgG4-mediated neurological autoimmune disorders. *Eur. J. Neurol.* **22**, 1151–1161
41. Derfuss, T., Linington, C., Hohlfeld, R., and Meinel, E. (2010) Axo-glial antigens as targets in multiple sclerosis: implications for axonal and grey matter injury. *J. Mol. Med.* **88**, 753–761
42. Popovich, P. G., Horner, P. J., Mullin, B. B., and Stokes, B. T. (1996) A quantitative spatial analysis of the blood-spinal cord barrier. I. Permeability changes after experimental spinal contusion injury. *Exp. Neurol.* **142**, 258–275
43. Noble, L. J., and Wrathall, J. R. (1989) Distribution and time course of protein extravasation in the rat spinal cord after contusive injury. *Brain Res.* **482**, 57–66
44. Schnell, L., Fearn, S., Schwab, M. E., Perry, V. H., and Anthony, D. C. (1999) Cytokine-induced acute inflammation in the brain and spinal cord. *J. Neuropathol Exp. Neurol.* **58**, 245–254
45. Schnell, L., Fearn, S., Klassen, H., Schwab, M. E., and Perry, V. H. (1999) Acute inflammatory responses to mechanical lesions in the CNS: differences between brain and spinal cord. *Eur. J. Neurosci.* **11**, 3648–3658
46. Zhou, X., He, X., and Ren, Y. (2014) Function of microglia and macrophages in secondary damage after spinal cord injury. *Neural Regen Res.* **9**, 1787–1795
47. Horner, P. J., Popovich, P. G., Mullin, B. B., and Stokes, B. T. (1996) A quantitative spatial analysis of the blood-spinal cord barrier. II. Permeability after intraspinal fetal transplantation. *Exp. Neurol.* **142**, 226–243
48. Perry, M. J., and Lawson, S. N. (1993) Neurofilaments in rat and cat spinal cord; a comparative immunocytochemical study of phosphorylated and non-phosphorylated subunits. *Cell Tissue Res.* **272**, 249–256
49. Perry, J. R., Deodhare, S. S., Bilbao, J. M., Murray, D., and Muller, P. (1993) The significance of spinal cord compression as the initial manifestation of lymphoma. *Neurosurgery* **32**, 157–162
50. Popovich, P. G., Wei, P., and Stokes, B. T. (1997) Cellular inflammatory response after spinal cord injury in Sprague-Dawley and Lewis rats. *J. Comp. Neurol.* **377**, 443–464
51. Streit, W. J., Semple-Rowland, S. L., Hurley, S. D., Miller, R. C., Popovich, P. G., and Stokes, B. T. (1998) Cytokine mRNA profiles in contused spinal cord and axotomized facial nucleus suggest a beneficial role for inflammation and gliosis. *Exp. Neurol.* **152**, 74–87
52. Zietlow, R., Dunnett, S. B., and Fawcett, J. W. (1999) The effect of microglia on embryonic dopaminergic neuronal survival in vitro: diffusible signals from neurons and glia change microglia from neurotoxic to neuroprotective. *Eur. J. Neurosci.* **11**, 1657–1667
53. Zhang, S. C., and Fedoroff, S. (1996) Neuron-microglia interactions in vitro. *Acta Neuropathol.* **91**, 385–395
54. Kurihara, D., Ueno, M., Tanaka, T., and Yamashita, T. (2010) Expression of galectin-1 in immune cells and glial cells after spinal cord injury. *Neurosci. Res.* **66**, 265–270
55. Villares, R., Cadenas, V., Lozano, M., Almonacid, L., Zaballos, A., Martinez, A. C., and Varona, R. (2009) CCR6 regulates EAE pathogenesis by controlling regulatory CD4+ T-cell recruitment to target tissues. *Eur. J. Immunol.* **39**, 1671–1681
56. Raposo, C., Graubardt, N., Cohen, M., Eitan, C., London, A., Berkutzki, T., and Schwartz, M. (2014) CNS repair requires both effector and regulatory T cells with distinct temporal and spatial profiles. *J. Neurosci.* **34**, 10141–10155
57. Austin, P. J., Kim, C. F., Perera, C. J., and Moalem-Taylor, G. (2012) Regulatory T cells attenuate neuropathic pain following peripheral nerve injury and experimental autoimmune neuritis. *Pain* **153**, 1916–1931
58. Blanco-Suarez, E., and Hanley, J. G. (2014) Distinct subunit-specific alpha-amino-3-hydroxy-5-methyl-4-isoxazolepropionic acid (AMPA) receptor trafficking mechanisms in cultured cortical and hippocampal neurons in response to oxygen and glucose deprivation. *J. Biol. Chem.* **289**, 4644–4651
59. Cizkova, D., Kakinohana, O., Kucharova, K., Marsala, S., Johe, K., Hazel, T., Hefferan, M. P., and Marsala, M. (2007) Functional recovery in rats with ischemic paraplegia after spinal grafting of human spinal stem cells. *Neuroscience* **147**, 546–560
60. Ankeny, D. P., and Popovich, P. G. (2010) B cells and autoantibodies: complex roles in CNS injury. *Trends Immunol.* **31**, 332–338
61. Ankeny, D. P., Guan, Z., and Popovich, P. G. (2009) B cells produce pathogenic antibodies and impair recovery after spinal cord injury in mice. *J. Clin. Invest.* **119**, 2990–2999
62. Gini, B., Lovato, L., Cianti, R., Cecotti, L., Marconi, S., Anghileri, E., Armini, A., Moretto, G., Bini, L., Ferracci, F., and Bonetti, B. (2008) Novel autoantigens recognized by CSF IgG from Hashimoto's encephalitis revealed by a proteomic approach. *J. Neuroimmunol.* **196**, 153–158
63. Huang, J., Sun, X., Mao, Y., Zhu, X., Zhang, P., Zhang, L., Du, J., and Qiu, X. (2008) Expression of immunoglobulin gene with classical V-(D)-J rearrangement in mouse brain neurons. *Int. J. Biochem. Cell Biol.* **40**, 1604–1615
64. Fehlings, M. G., and Nguyen, D. H. (2010) Immunoglobulin G: a potential treatment to attenuate neuroinflammation following spinal cord injury. *J. Clin. Immunol.* **30 Supplemental 1**, S109–S112
65. Kobeissy, F., and Moshourab, R. A. (2015) Autoantibodies in CNS Trauma and Neuropsychiatric Disorders: A New Generation of Biomarkers. In: Kobeissy, F. H., ed. *Brain Neurotrauma: Molecular, Neuropsychological, and Rehabilitation Aspects*, Boca Raton (FL)